buildings

MDPI

Article

RNN Architecture-Based Short-Term Forecasting Framework for Rooftop PV Surplus to Enable Smart Energy Scheduling in Micro-Residential Communities

Abdo Abdullah Ahmed Gassar [1,2,*], Mohammad Nazififard [2] and Erwin Franquet [2]

[1] Université Clermont Auvergne, Clermont Auvergne INP, CNRS, Institut Pascal, F-63000 Clermont–Ferrand, France
[2] Laboratoire Polytech'Lab (POLYTECH'LAB), Université Côte d'Azur, Polytech Nice Sophia, BP 145, Sophia Antipolis, 06903 Vallauris, France
* Correspondence: gassar@khu.ac.kr or abdo.gassar@uca.fr

Abstract

With growing community awareness of greenhouse gas emissions and their environmental consequences, distributed rooftop photovoltaic (PV) systems have emerged as a sustainable energy alternative in residential settings. However, the high penetration of these systems without effective operational strategies poses significant challenges for local distribution grids. Specifically, the estimation of surplus energy production from these systems, closely linked to complex outdoor weather conditions and seasonal fluctuations, often lacks an accurate forecasting approach to effectively capture the temporal dynamics of system output during peak periods. In response, this study proposes a recurrent neural network (RNN)- based forecasting framework to predict rooftop PV surplus in the context of micro-residential communities over time horizons not exceeding 48 h. The framework includes standard RNN, long short-term memory (LSTM), bidirectional LSTM (BiLSTM), and gated recurrent unit (GRU) networks. In this context, the study employed estimated surplus energy datasets from six single-family detached houses, along with weather-related variables and seasonal patterns, to evaluate the framework's effectiveness. Results demonstrated the significant effectiveness of all framework models in forecasting surplus energy across seasonal scenarios, with low MAPE values of up to 3.02% and 3.59% over 24-h and 48-h horizons, respectively. Simultaneously, BiLSTM models consistently demonstrated a higher capacity to capture surplus energy fluctuations during peak periods than their counterparts. Overall, the developed data-driven framework demonstrates potential to enable short-term smart energy scheduling in micro-residential communities, supporting electric vehicle charging from single-family detached houses through efficient rooftop PV systems. It also provides decision-making insights for evaluating renewable energy contributions in the residential sector.

Keywords: RNN architecture; surplus energy forecasting; smart energy scheduling; EV charging optimization; micro-residential community

Check for updates

Received: 30 November 2025
Revised: 3 January 2026
Accepted: 13 January 2026
Published: 17 January 2026

Copyright: © 2026 by the authors. Licensee MDPI, Basel, Switzerland. This article is an open access article distributed under the terms and conditions of the Creative Commons Attribution (CC BY) license.

1. Introduction

Growing awareness of greenhouse gas emissions and their environmental consequences, particularly within residential communities, has accelerated the adoption of distributed solar photovoltaic (PV) systems and electric vehicles (EVs) as sustainable alternatives in recent years. Both technologies are expected to play a pivotal role in shaping

the future energy landscape [1]. According to the International Energy Agency (IEA), the global number of EVs on the road is expected to reach 145 million by 2030 [2], while approximately 100 million residential units are projected to be equipped with rooftop solar PV systems within the same period [3]. However, the currently growing penetration of these technologies in residential units without proper integration strategies poses significant operational challenges to distribution grids. These challenges arise primarily from the temporal mismatch between onsite PV generation and household energy demand on one hand, and between household demand and potential surplus energy availability during certain times of the year on the other [4]. In addition, the growing demand for energy to charge EVs, which are often integrated directly into residential energy systems, further exacerbates these issues [5]. Among the potential issues, the misalignment between onsite generation and demand in residential units can result in voltage deviations, equipment overloads, increased power losses, and overall threats to the stability of the distribution grid [6,7]. Without effective integration strategies, these adverse impacts may hinder the widespread adoption of PV and EV technologies, while minimizing the relevant benefits and delaying the transition toward sustainable, low-carbon energy systems in residential communities.

In the context of these challenges, integrating onsite PV self-generation, EV charging, residential demand, and grid power into a coordinated system presents a promising pathway for enhancing energy resilience and efficiency in residential communities. The principle of achieving such a coordinated system lies in creating a dynamic synergy that aligns real-time onsite PV generation with residential loads, including EV charging demand, thereby maximizing the utilization of locally generated renewable energy and minimizing dependency on the grid [4,8]. However, achieving this synergy hinges on the availability of accurate estimates for three key variables: onsite PV self-generation, energy demand, and potential surplus energy during times when onsite generation peaks while demand is at its lowest [9]. In the case of energy surplus estimates, it is imperative to understand and quantify the dynamic energy balances between the community-scale building demands and their onsite generation capabilities [10]. This task is complicated by factors such as unpredictable occupancy patterns and fluctuating outdoor environmental conditions, both of which significantly influence energy demand and generation profiles [11]. Therefore, strengthening the role of community-scale building energy modeling is a crucial component for effectively enabling the dynamic synergy required to integrate and operate these technologies within residential communities. In this context, creating precise models is vital to support coordinated energy systems and informed decision-making, optimize energy usage, and ensure the long-term sustainability of residential community developments [12,13].

Community-scale building energy prediction methods are commonly classified as physics-based, data-driven, and hybrid models. Physics-based models are recognized for their predictive accuracy and high interpretability; however, their limitations often stem from inherent complexity and the considerable time required for development [14]. These limitations are more pronounced in large-scale or complex building systems. Hybrid models integrate physical principles and historical data to improve prediction accuracy. However, they present challenges, primarily due to their technical complexity and the specialized expertise required for implementation. Data-driven models, based on artificial intelligence, have increasingly gained prominence in building energy applications due to their simplicity, flexibility, and reduced reliance on detailed physical information [15]. These models are particularly effective at addressing system complexities in energy demand and supply predictions, especially in handling nonlinear relationships and dynamic fluctuations in time-series data [16,17]. Several common data-driven models used in this domain include Random Forests (RF), Extreme Gradient Boosting (XGB), Support Vector Regression (SVR), and Artificial Neural Networks (ANN) [18]. These models demonstrate acceptable

capabilities for learning from time-series datasets, adapting to dynamic patterns, and producing highly accurate predictions, making them preferred choices for advanced load and generation forecasting in community-scale building energy research.

In parallel, load and PV generation forecasts in buildings are broadly categorized by forecast horizon and intended purpose into four types: very short-term, short-term, medium-term, and long-term. Very short-term forecasting ranges from a few seconds to one hour; short-term forecasting spans several hours to a few days (up to a week); medium-term forecasting covers a few weeks to several months; and long-term forecasting typically extends beyond one year [19,20]. In micro-residential community contexts, where scalable surplus energy management is critical, short-term forecasting is used to balance the supply of electric power and load demand, serving as an essential tool for scheduling onsite power generation and laying the foundation for energy dispatch and administration [21]. Therefore, the availability of accurate short-term forecasts of the surplus energy variable enables optimal EV charging schedules that prioritize the use of available surplus energy, thereby enhancing system-wide energy self-sufficiency and grid stability [22]. Accurate short-term forecasts account for the dynamic interplay of meteorological variables, including cloud cover and seasonal fluctuations, which significantly affect PV generation. This necessitates the development of reliable models capable of capturing both short-term variations and broader trends [23]. These models leverage historical time-series data on PV self-generation and residential energy demand, along with outdoor environmental factors, to produce reliable predictions of surplus energy aligned with temporal and seasonal patterns. Such forecasting supports the effective coordination of energy use by optimizing surplus energy allocation for micro-residential community-scale EV charging while maintaining distribution grid stability.

Despite extensive research on onsite PV generation [19,23] and PV-load forecasting [24,25], limited attention has been given to forecasting surplus energy availability, particularly in the context of residential communities. Among renewable sources, solar energy has been identified as having the greatest impact on increasing surplus energy levels. While many studies support this observation in PV applications, Elbeh and Sleiti [26], by optimizing a concentrated solar plant, observed that the amount of surplus energy during the summer months can exceed 80% in the absence of proper energy management strategies. Furthermore, surplus levels exceeding 10% are typically indicative of suboptimal energy efficiency in a renewable energy system [27]. Surplus energy can still pose a challenge even in urban areas with full access to the synchronous energy grid. In grid-connected systems, high volumes of surplus energy may strain low-voltage networks, particularly when they are integrated with large-scale community renewable energy systems. In micro-residential community settings, this gap is particularly critical due to the small-scale nature of these systems and the substantial influence of individual household behaviors [28]. The most applicable solution to address this issue is provided by accurate short-term predictions, not exceeding 48 h, for surplus energy availability in the context of these micro-residential communities. To achieve this, this study proposes an RNN architecture-based approach, specifically employing long short-term memory (LSTM), gated recurrent unit (GRU), bidirectional LSTM (BiLSTM), and standard recurrent neural networks (RNN). These architectures outperform traditional methods, such as multiple linear regression (MLR) and autoregressive integrated moving average (ARIMA), by accurately capturing short-term variability and modeling nonlinear dependencies between onsite PV generation and household demand, which reflect the unique behavioral dynamics of micro-communities [29,30]. This capability is particularly important because onsite PV generation is inherently nonlinear, governed by fluctuations in outdoor weather conditions. By leveraging these architectures, this approach facilitates the synchronization of EV charging with periods of maximum surplus

energy, thereby optimizing renewable self-consumption, minimizing grid dependency, and enhancing overall energy efficiency. The novelty of this study lies in explicitly targeting surplus energy forecasting for single-family detached houses within micro-residential communities, thereby addressing a critical research gap overlooked in prior studies.

2. Related Previous Studies and Gaps

In the existing literature, several studies have examined various operational strategies for managing community-scale energy systems [31,32] under different energy trading modes, including peer-to-peer (P2P) and peer-to-grid (P2G) approaches. In parallel, other considerable attention has been given to the integration of EVs into these systems [33,34], exploring different charging paradigms, such as vehicle-to-home (V2H) and vehicle-to-grid (V2G). While these studies have contributed valuable insights into decentralized energy management and economic optimization, they often rely on simplified or static representations of surplus energy and assume idealized user behaviors or profiles of the energy availability. For instance, Li and Ma [35] analyzed P2P electricity trading in grid-connected community houses, some of which are integrated with distributed PV systems. However, they assumed idealized energy consumption patterns and user behaviors, which may not reflect the variability of real-world onsite PV generation and household demand. Similarly, Robledo et al. [36] studied EV and V2G integration within active distribution networks, but used simplified surplus PV energy models, which may neglect the dynamic nature of PV generation and its interaction with user behavior and charging demands. While such studies demonstrate the potential of EV-grid coordination, their reliance on static assumptions regarding surplus energy availability overlooks a critical complexity: the stochastic interplay among onsite PV generation, household consumption, and EV charging patterns.

In addition, Table 1 presents recent studies on energy surplus predictions. Zahedi et al. [37] developed a GRU-based model to predict surplus energy availability in a residential community composed of 13 buildings, aiming to allocate the surplus for EV charging. While the use of GRU networks highlights the potential of data-driven models, the study relies on fixed PV generation and load profiles, assuming consistent daily patterns and predefined charging cycles. More importantly, the load profile was calculated for a single building and extrapolated across the community, limiting the model's capacity to reflect building-level variability and dynamic household behaviors. These simplifications reduce the model's effectiveness in capturing real-time fluctuations driven by stochastic weather and occupant behavior, both critical for surplus energy forecasting in micro-residential contexts. Falces et al. [38] also developed a comparative framework using four data-driven methods, including random forest (RF), extreme gradient boosting (XGB), support vector regression (SVR), and cubist (CUB), to forecast total load, onsite PV generation, and net load under varying PV penetration scenarios (0%, 17.8% and 35.6%). Their findings indicated that both direct and indirect forecasting models can achieve comparable accuracy, offering practical value for grid operators, particularly when behind-the-meter PV data is unavailable. However, the study focuses on net load rather than surplus energy, which in this context is defined as PV generation exceeding household energy demand. Moreover, while traditional models such as SVR and RF are effective for general pattern recognition, they often lack the capability to capture the temporal dependencies inherent in surplus energy data, potentially limiting their accuracy in high-resolution forecasting within dynamic residential settings.

Table 1. Comparison of the proposed methods with other research works on forecasting surplus energy.

	Parameters in Forecast Formulation			Temporal Granularity	Proposed Approach
	Load	PV	Surplus		
Zahedi et al. [37]	-	-	✔	Hourly	GRU
Falces et al. [38]	-	-	✔	Hourly	FR, XGB, CUB, SVR
Tharumaraja et al. [39]	-	✔		Hourly	LSTM
Dias et al. [40]	-	-	✔	Hourly	MLR
Eze et al. [41]	-	✔	✔	Hourly	Simulation model
Liao et al. [42]	-	-	✔	Hourly	Simulation model
Bhatti and Williams [43]	-	-	✔	Hourly	Statistics
This study	✔	✔	✔	Hourly	RNN, BiLSTM, LSTM, GRU

On the other hand, Tharumaraja et al. [39] proposed using an LSTM network to forecast available PV energy generation from renewable-integrated households, focusing on very short-term surplus energy predictions for trading within a microgrid. Dias et al. [40] developed an MLR-based model to forecast surplus energy generation for residential loads managed via smart plugs, using data from 11 households in southern Germany. The study demonstrated that both hourly and daily MLR forecasts achieved high accuracy in optimizing local energy use. However, the model's reliance on linear assumptions limits its capability to capture the nonlinear and spatiotemporal complexities of PV generation and household demand dynamics. Eze et al. [41] developed simulation models that utilize surplus energy to operate an inter-seasonal heating and cooling system connected to an underground thermal energy storage. Similarly, Liao et al. [42] used a model combining a vector-based solar radiation model and electricity consumption profiling to quantify urban-scale PV surplus in Seoul, aiming to identify when and where PV surplus occurs. Bhatti and Williams [43] proposed a statistical approach to estimate surplus solar energy in off-grid solar home systems in rural India using detailed, sensor-based load and solar data at various time resolutions. While these works identify surplus energy patterns, the availability of real-time surplus energy data remains a key constraint. Consequently, the comparative effectiveness of various modeling approaches for short-term surplus energy forecasting in decentralized systems remains an open and underexplored question. To address this gap, an RNN architecture-based short-term forecasting framework for net surplus energy is essential to enable responsive and efficient energy scheduling, particularly in micro-residential communities, where infrastructure limitations and high occupancy densities heighten the need for accurate energy balance management.

Contributions and Paper Structure

The paper contributes to the literature by: (1) proposing an advanced deep learning approach based on RNN architectures to provide accurate short-term forecasts of residential surplus energy availability, which is more challenging than PV or load forecasting alone due to the combined variability of both generation and consumption, as well as the complex behavioral dynamics of households, thereby maximizing the utilization of surplus energy to charge community-scale EVs instead of exporting it to the grid or storing it in batteries; (2) evaluating the effectiveness of the proposed forecasting models using different volumes of data and features to capture short-term fluctuations and nonlinear dependencies in micro-residential community energy profiles. In addition, the proposed

framework explicitly introduces dual temporal balancing scenarios (24 h demand–24 h generation and 48 h demand–24 h generation) and seasonal segmentation to better capture intra-annual variability in surplus energy availability. Although the case study involves six single-family detached houses, these are treated as a representative micro-residential community, and the proposed surplus forecasting framework is fully scalable to larger residential clusters. (3) presenting a comprehensive performance comparison with prediction models from previous studies (Table 1), applied to short-term forecasting tasks not exceeding 48 h, under different scenario profiles of micro-residential community-scale surplus energy data, as it allows households to schedule charging around predicted surplus peaks while avoiding grid overloads; and (4) contributing to the growing body of research on intelligent energy management systems in micro-residential communities by enabling more sustainable energy practices, supporting seamless EV integration, and providing a framework that can be generalized to other climates or larger communities by retraining the models with locally relevant PV generation and consumption data.

The remainder of the paper is structured as follows: Section 3 describes the methodology, including the RNN architectures, forecast model development, and performance evaluation metrics. Section 4 presents and discusses the results in comparison with traditional and commonly used data-driven forecasting models, while Section 5 concludes the study and summarizes potential future research directions.

3. Methodology

The research methodology is implemented through five carefully designed steps, as shown in Figure 1, with the objective of enabling short-term forecasting of surplus energy to support optimal EV charging strategies in the context of a micro-residential community. Step 1 defines a representative micro-residential community in an urban context, incorporating scalable rooftop PV systems and reflecting a realistic distributed self-generation potential (Section 3.1). Step 2 consists of generating source datasets within a simulation and analysis framework, calibrated to the same weather conditions as the target residential buildings, followed by processing high-resolution datasets on energy demand and onsite PV self-generation for the community. Step 3 compares each household's energy demand with its self-generation to quantify available surplus energy within the micro-residential community. Accordingly, this surplus is calculated under two temporal balancing scenarios: 24-h demand versus 24-h generation, and 48-h demand versus 24-h generation. This forms the foundation for assessing flexibility in EV charging operations, as detailed in Section 3.2. All datasets undergo preprocessing to convert them into suitable formats for subsequent analysis. In Step 4, correlation-based feature selection [44,45] is used to select input variables for the forecasting models by estimating the correlation coefficients between different energy profiles and each input feature, an essential step to enhance model accuracy. Subsequently, short-term forecasting models are developed to capture the temporal dynamics of baseline energy demand and self-generation. This process involves in-depth hyperparameter tuning within the deep learning framework to determine the best-performing parameter settings (optimal parameter values). These optimized parameters are then incorporated to enhance the prediction accuracy of the forecasting model. Following this, the baseline forecasting model is updated with surplus energy availability data, applying the refined hyperparameters to improve the precision of future surplus energy predictions. In Step 5, the model undergoes testing and validation to assess the reliability of community-scale surplus energy forecasts. This evaluation includes a comparative analysis of RNN-based deep learning models and commonly used data-driven models to investigate the effectiveness of RNN-based models. The following

subsections detail the five steps, explaining the methodologies and analytical procedures employed to fulfill the study's objectives.

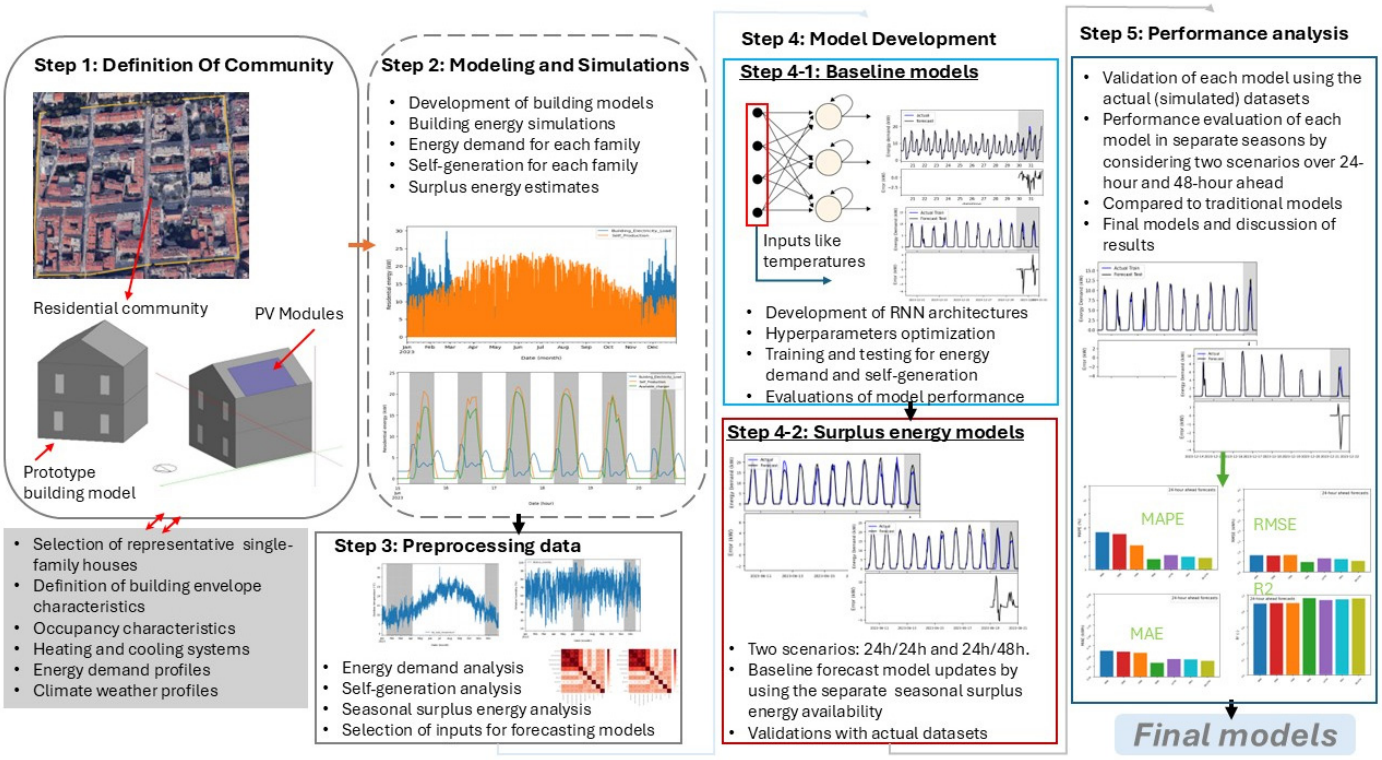


Figure 1. Research methodology workflow used in this study.

3.1. Representative Micro-Residential Community Case Study

To investigate the performance of the proposed RNN-based approach in forecasting short-term surplus energy, six single-family detached houses located in the Carré d'Or neighborhood of the city of Nice were selected as a realistic micro-residential community case study. Particularly, this type of house represents a significant portion of the French residential sector, approximately 21% [46], and is typically designed to accommodate medium-sized families of three to six members, with a layout comprising a main living room, three bedrooms, a shared bathroom, and a kitchen, as illustrated in Figure 2. Each house is a two-story structure with a total floor area of 102.4 m^2 and reflects a popular, scalable micro-residential configuration. The buildings were selected due to their homogeneity in terms of architectural typology, occupancy patterns, and energy system configurations, which are key factors for analyzing short-term energy dynamics in a representative and scalable environment. Notably, these houses typically rely on natural ventilation and lack mechanical cooling systems [46,47], which enhances energy sufficiency and supports optimized EV charging scenarios using surplus energy from rooftop PV systems. Further details of the building configurations are summarized in Table 2.

To extrapolate the energy demand profiles of these houses within the micro-residential community context, this study employed DesignBuilder® (Version 7.3.1.003), a dynamic energy simulation software that serves a graphical interface for EnergyPlus (Version 9.4) [48,49]. It was selected primarily for its proven accuracy in simulating residential energy behavior and PV generation, along with its user-friendly interface and seamless integration with EnergyPlus, offering a balance between model fidelity and computational efficiency compared with other commonly used BEM tools. DesignBuilder was used to define baseline prototype models and perform detailed energy simulations of each house structure. The simulations accounted for lighting, heating, domestic hot water, and appli-

ance usage, while cooling demand was excluded due to the absence of cooling systems in these buildings.

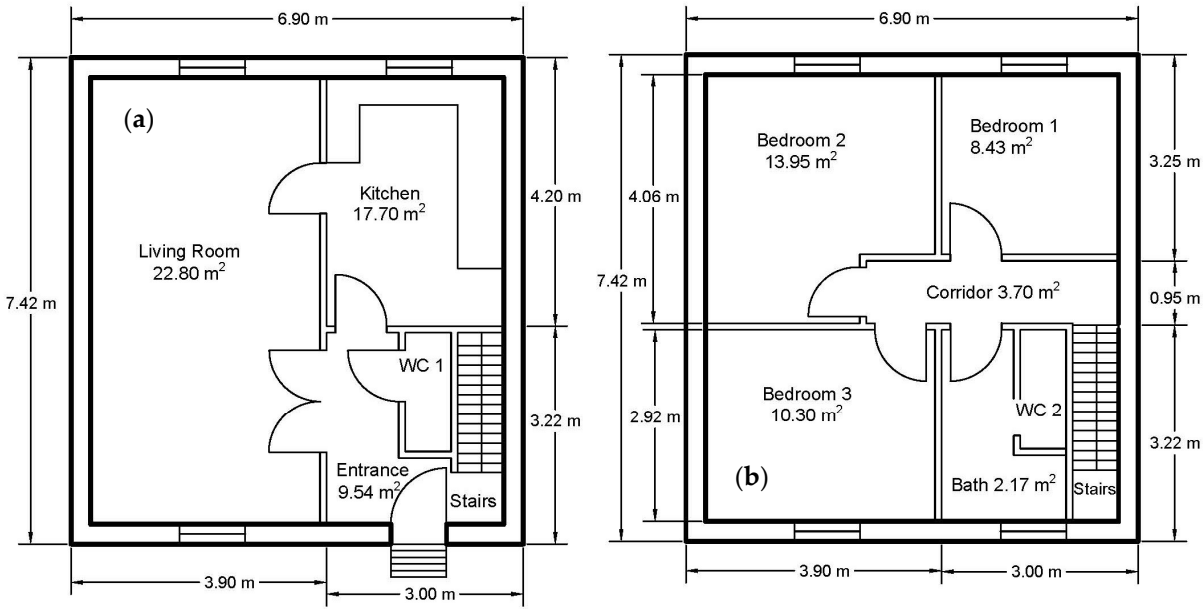


Figure 2. Layout of the single-family detached house in the targeted micro-residential community: (**a**) ground floor and (**b**) first floor.

Table 2. Details of the considered single-family detached house typology.

Component	Description
Overall house area (net and gross area)	102.4 m^2, 115.52 m^2
Footprint	6.90 mm by 7.42 m, a two-story house
Window area (window openings)	5% (Window-to-wall ratio)
Exterior wall construction	(0.01 m) Gypsum board + (0.11 m) brick + (0.01 m) timber sliding
Floor construction	(0.05 m) soil-leveling layers + (0.2 m) cast concrete + (0.2 m) timber floor
Type and construction of the roof	Pitched roof: (0.025 m) Clay tile+ (0.02 m) Air gap + (0.2 m) Timber flooring + (0.02 m) Plaster board
Glazing and the type of windows	Single-glazed (0.006 m) clear glass with a wooden frame vertical divider
Ventilation system	Natural ventilation using operable windows
Lighting system	General lighting system provided
Heating system	Electric radiators with a coefficient of performance (CoP-1)
Cooling system	Not used
Domestic hot water system	As part of the heating system
Infiltration rate	1.0 ACH (air change per hour)
Shading devices	No external shading devices provided

The primary objective of these simulations was to generate test datasets within a representative community context for implementing RNN models (Sections 3.3 and 3.6). Each single-family detached house was modeled individually to produce high-resolution energy demand profiles under actual weather conditions using local climate data, closely reflecting realistic operating conditions within a representative micro-residential community. Figure A1 (Appendix A) presents a 3D representation of the prototype single-family

detached house model used in the simulations. The building characteristics, as defined by the French Puccini house configuration for a standard single-family detached house, are captured in Table 2 and referenced in [46,50]. The prototype represents a two-story, single-family house divided into two thermal zones, with a total conditioned floor area of 102.4 m^2. The glazing area, consistent with the Puccini layout, accounts for approximately 5% of the façade area on each floor.

The heating system integrated into the original prototype residential model consists of electric radiators. This system features simple electric resistance heating coils, operating with a coefficient of performance (CoP) of 1 for both space heating and domestic hot water production, serving all thermal zones of each house. Natural ventilation is modeled through occupant-driven window opening, with an air permeability rate of 1.0 ACH (air changes per hour) to account for infiltration through leaks and cracks. All simulation input values were adopted directly from the original version of prototype models without modifications.

To simulate the rooftop PV systems of each house and accurately forecast onsite energy generation within the community, this study employed the Solar Collector model integrated within the DesignBuilder–EnergyPlus environment. Based on equations from ASHRAE standards and the methodology of Duffie and Beckman (1991) [51], the Solar Collector estimates the energy output of the building-attached PV systems using a set of straightforward input parameters. It supports two configurations: (1) Simple and (2) Equivalent One-Diode. This model's integration in DesignBuilder enables hourly estimation of on-site PV generation [52]. For this study, a rated PV DC (direct current) capacity of 2.88 kWp was specified, along with an inverter efficiency of 96%. The Equivalent One-Diode model was selected, incorporating a 15% module efficiency, a direct current electrical bus with an inverter, and monocrystalline solar cells. As shown in Figure A1 (Appendix A), the PV array is mounted on both south- and north-facing roof slopes of the prototype single-family detached house. The placement and orientation of the modules are chosen to reflect the building's design specifications and realistic conditions. The number of PV modules in the model also matches the actual size and layout of the PV system planned for the target domain.

Figure 3 illustrates the typical climate conditions for the area studied in Nice, France, which is characterized by Mediterranean climatic conditions. The dataset captures daily averages of key meteorological variables, including horizontal global irradiation (Wh/m^2), diffuse solar radiation (Wh/m^2), direct normal solar radiation (Wh/m^2), and dry bulb temperature (°C). The district exhibits a Mediterranean climate, marked by pronounced seasonal shifts, with summer temperatures ranging from 16 to 35 °C and winter temperatures from 0 °C to 14 °C. Solar irradiation patterns follow a clear seasonal trend, with peak GHI values (roughly 800 Wh/m^2) occurring in May, indicating optimal solar harvesting potential during late spring. These climate dynamics are vital for precise energy modeling, enabling balanced assessments of building energy demand versus onsite renewable generation capacity. Based on the prevailing climate data, this study conducted annual simulations of whole-building energy performance alongside on-site energy generation. These outputs were then analyzed through a supply–demand balance assessment, and the results were classified into distinct categories according to similarities in energy demand and generation patterns. This approach allowed a more organized and in-depth evaluation by identifying representative energy profiles across different seasonal periods throughout the year. Additional details on the surplus energy analysis are provided in Section 3.2.

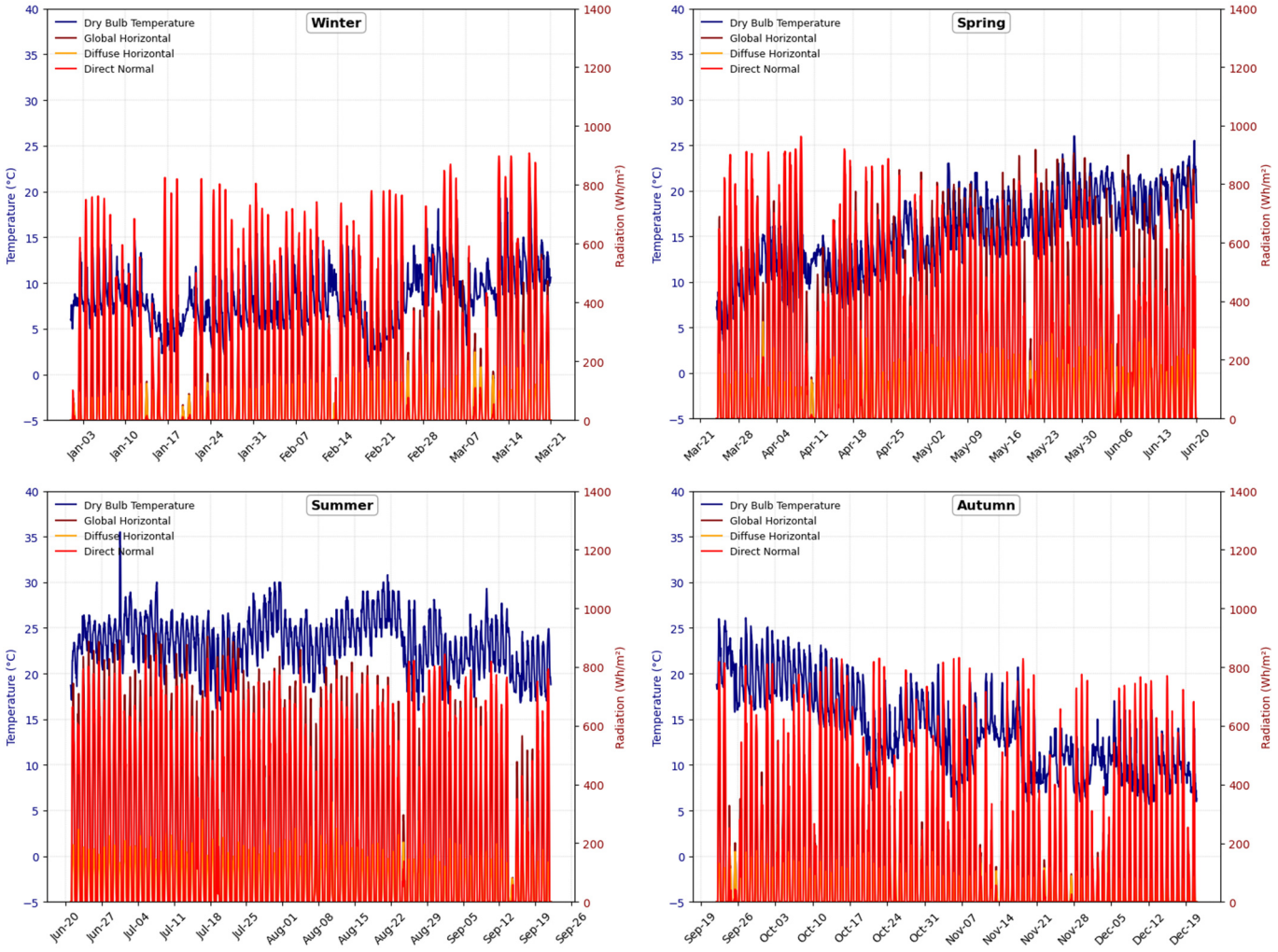


Figure 3. Seasonal climate conditions at the location of the proposed micro-residential community, used for annual whole-house simulations.

3.2. Community-Scale Surplus Energy Estimation Scenarios

As previously outlined, the purpose of this study is to develop an advanced data-driven framework based on RNN architectures to predict the future aggregated surplus energy of single-family detached houses connected to the local power grid within a micro-residential community. The primary objective is to effectively enable optimization and management of EV charging schedules using these surplus energy forecasts. In line with the proposed data-driven framework, the first step is to determine the baseline energy consumption profile of each house in the community. This profile serves as a reference for calculating the net surplus energy by comparing household demand with onsite self-generation from distributed rooftop PV systems. In this study, EV charging windows were defined based on typical household occupancy patterns and user behavior, combined with periods of predicted surplus PV energy availability, thereby ensuring alignment between energy generation and charging demand. The total baseline energy consumption of each single-family detached house in the community at each time step t is calculated as follows:

$$E_{load,i}(t) = E_{heating,i}(t) + E_{appliances,i}(t) + E_{lighting,i}(t) \quad (1)$$

where $E_{heating,i}(t)$, $E_{applainces,i}(t)$, and $E_{lighting,i}(t)$, represent the space heating demand, the energy consumption by household appliances, and the lighting energy use for each house i in the community during hour t, respectively.

Following the identification of baseline consumption, the instantaneous surplus energy for each detached single-family house i at time step t is computed by subtracting its total energy demand from the onsite energy generated by its distributed rooftop PV systems, as shown in Equation (2). This step enables the detection of time-dependent surpluses or deficits in surplus energy availability at the level of individual houses across different seasons of the year.

$$SE_i(t) = E_{gen,i}(t) - E_{load,i}(t) \quad (2)$$

where $SE_i(t)$ is the surplus energy (kWh) of house i at time t; $E_{gen,i}(t)$ is the PV self-generated energy of house i for every hour t; and $E_{load,i}(t)$ is the total fixed baseline energy consumption of house i for every hour t. Figure 4 presents the total annual hourly energy consumption and corresponding self-generation at both the individual house (Figure 4a) and community levels (Figure 4b). As observed, a substantial portion of surplus energy is available throughout the year, presenting a valuable opportunity for its utilization in charging community-scale EVs.

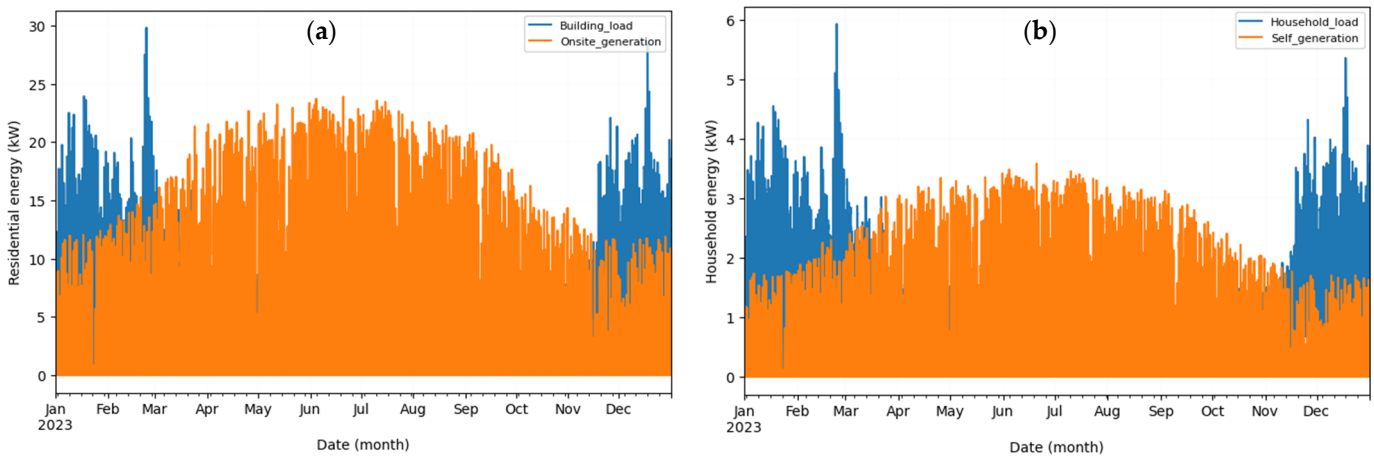


Figure 4. Energy demand and onsite energy generation of distributed PV systems on rooftops: (**a**) the community-level and (**b**) the single-family house-level.

To maximize surplus energy utilization at the micro-residential community level, the surplus energy values from each of the N houses are aggregated at each time step t, as expressed in Equation (3). This aggregation allows for the characterization of time-dependent, community-wide surplus energy patterns, thereby supporting coordinated EV charging or grid injection strategies.

$$SE_{community}(t) = \sum_{i=1}^{N} E_{surplus,i}(t) \quad (3)$$

Based on the obtained surplus energy patterns and the objective of developing accurate short-term forecasting models, two distinct surplus energy estimation scenarios are considered, as described in Equations (4) and (5). In both scenarios (Figures 5 and 6), surplus energy is derived by aggregating the individual surplus values, which occur between 6:00 AM and 8:00 PM, from all N single-family detached houses at each time step t. In the first scenario (24-h to 24-h Aggregation), shown in Equation (4), the community-scale surplus energy is calculated by aggregating, across all N houses, the difference between total PV energy generated and total energy consumed within a fixed 24-h period, representing a day-ahead surplus estimation under equal forecasting horizons. In contrast, Equation (5) represents the second scenario (24-h to 48-h Aggregation), where the surplus energy is computed by comparing 24 h of onsite PV generation with 48 h of household demand. This extended-horizon scenario is implemented by using the observed PV generation and

energy demand from one day to assess surplus availability over the subsequent two-day period. It enables proactive EV charging and load management by providing advanced insight into energy availability beyond the conventional 24-h forecast, thereby supporting more flexible and optimized scheduling decisions. This scenario also allows for evaluating how a single day's energy generation could support demand over a longer time horizon, which is an important consideration for mid-term EV charging strategies.

$$SE_{community}^{(24\to24)}(t) = \sum_{i=1}^{N} E_{surplus,i}(t) = \sum_{i=1}^{N}\left[E_{gen,i}^{(24h)} - E_{load,i}^{(24)}\right] \quad (4)$$

$$SE_{community}^{(24\to48)}(t) = \sum_{i=1}^{N} E_{surplus,i}(t) = \sum_{i=1}^{N}\left[E_{gen,i}^{(24h)} - E_{load,i}^{(48)}\right] \quad (5)$$

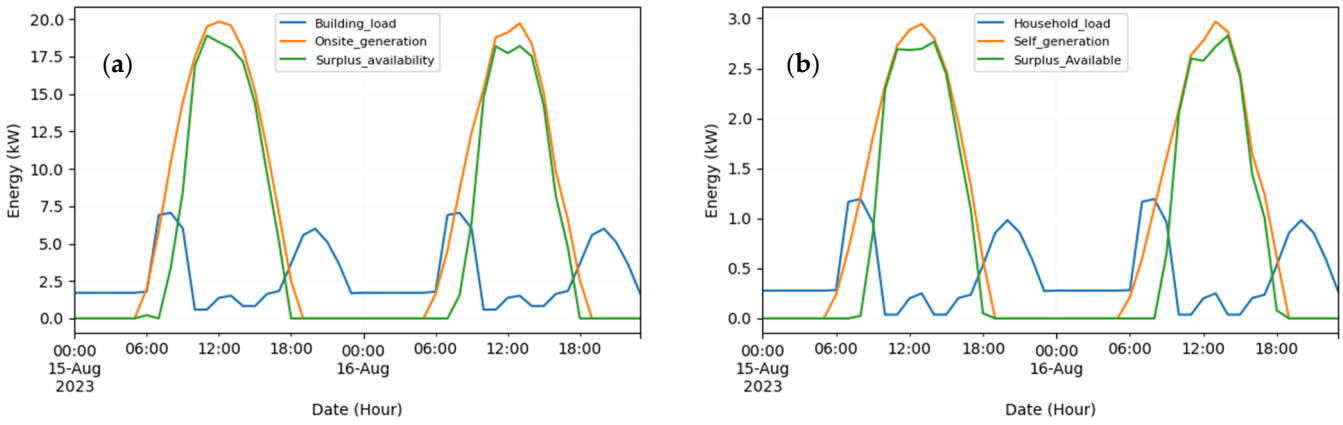


Figure 5. Surplus estimation scenario (24 h to 24 h) for a typical two-day period in summer: (**a**) the community-level and (**b**) the household-level.

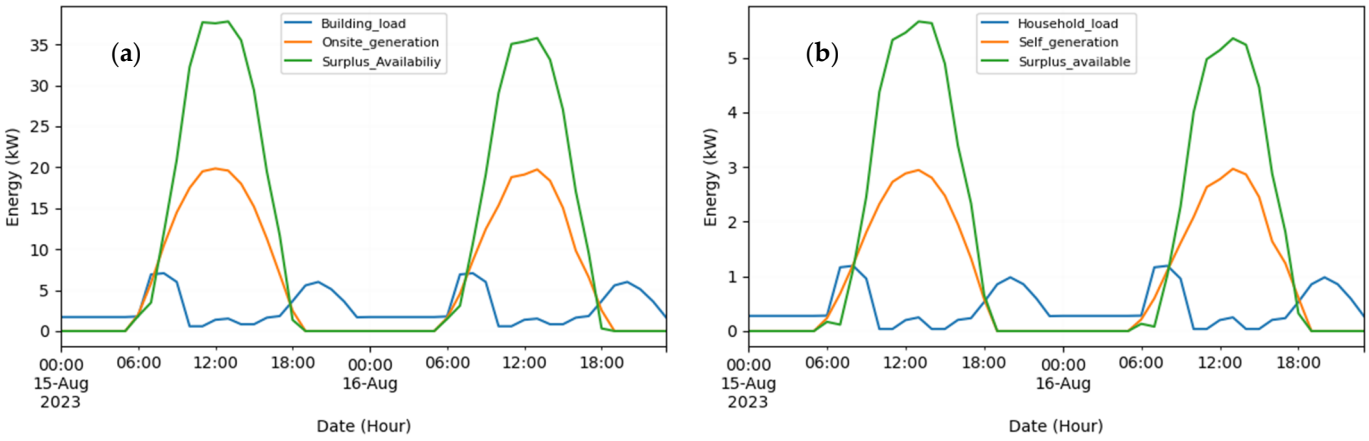


Figure 6. Surplus estimation scenario (24 h to 48 h) for a typical two-day period in summer: (**a**) the community-level and (**b**) the household-level.

Accordingly, this community-level surplus signal serves as the target variable for the RNN-based forecasting models. The objective is to learn a mapping function f_θ that predicts surplus energy over a specified future horizon H, based on historical observations:

$$\hat{SE}_{community}(t+h) = f_\theta(X_{t-w+1:t}),\ h = 1,2,\ldots,\ H \quad (6)$$

In this formulation, $\hat{SE}_{community}(t+h)$ denotes the forecasted surplus energy at future time $t+h$, $(X_{t-w+1:t})$ is the input sequence of historical features (input variables) over a window of length w, f_θ represents the RNN model parameterized by θ, and H defines the forecast horizon, which is 24 or 48 h ahead. Because PV forecast uncertainty increases

significantly beyond one day, in the 48 h demand–24 h generation scenario, PV generation is fixed to a 24-h horizon to reflect realistic operational constraints. Extending the load horizon to 48 h under this constraint allows evaluation of EV charging flexibility and surplus allocation, which is representative of day-ahead residential energy scheduling. Once the surplus energy profiles are forecasted using RNN models, they are mapped into typical EV charging windows. These are defined as the periods during which EVs are expected to be parked and available for charging.

Aligning the forecasted energy surplus with these windows enables intelligent and proactive charging control. The optimal charging window, $W_{optimal}$, is defined as follows:

$$W_{optimal} = \left\{ t \in W_{EV}(t) \mid E_{community}(t) > 0 \right\} \tag{7}$$

where $W_{EV}(t)$ denotes the time periods when EVs are connected to chargers. This mapping ensures that EVs are charged preferentially during surplus periods, minimizing grid dependency and maximizing the use of locally generated renewable energy. Figures 5 and 6 illustrate the surplus energy patterns over four days of expected charging cycles for both 24-h and 48-h scenarios. As shown, charging schedules are aligned with periods when the gap between local onsite generation and household demand is at its maximum. By leveraging historical surplus data (generated by EnergyPlus integrated with DesignBuilder), the RNN-based approach forecasts optimal charging times for the upcoming days. These forecasts are critical for establishing proactive EV charging schedules that support local energy autonomy and reduce reliance on the external grid.

3.3. RNN Architecture-Based Framework

3.3.1. Recurrent Neural Network

To forecast the community-scale surplus energy signal $\hat{SE}_{community}(t+h)$ defined in Equation (6), a recurrent neural network (RNN) is employed as the predictive model. RNNs, a class of advanced deep learning models, are well-suited for time-series forecasting tasks due to their ability to retain information from previous time steps through their internal memory recurrent structure, known as the hidden state, which dynamically evolves over time. Thanks to the change in its structure, it allows the outputs of a previous layer to become the inputs of a current layer, thus generating a compact model representation for sequential input data [53]. This structure makes them particularly effective for capturing short-term temporal dependences in dynamic community-scale energy data, including building demand, PV generation, and surplus energy. Figure A2a in Appendix A depicts the recurrent structure of a single RNN unit, which is composed of input layers accepting sequences with shape ($\{w, d\}$: where w is the time window size and d is the number of input features), stacked recurrent layers with a hidden size n, and a final dense layer for outputting the forecast over the next H time steps.

At each time step t, the RNN updates its hidden state h_t based on the current input x_t and the previous hidden state h_{t-1}, as defined by Equations (8) and (9):

$$h_t = \sigma(W_{xh}x_t + W_{hh}h_{t-1} + b_h) \tag{8}$$

$$\hat{y}_t = W_{hy}h_t + b_y \tag{9}$$

Here, x_t, h_t, σ, and $\hat{y}_t$ denote the input feature vector at time t, the hidden state, the nonlinear activation function (tanh/ReLU), and the forecasted surplus energy for a single-step ahead, respectively. The terms W_{xh}, W_{hh}, W_{hy} and b_h, b_y represent trainable weight matrices and learnable biases. To optimally implement the time-series forecasting task, the full multivariate time-series history is converted into samples using a moving window procedure described in [54]. This process generates input-output pairs for training.

Specifically, the model input is a multivariate sequence $x_{t-w+1:t} \in \mathbb{R}^{w+d}$, where w is the historical window length (set to 24 timesteps in this study), and d is the number of input features, as detailed in Section 3.5. The objective is to learn a mapping function f_θ that accurately forecasts surplus energy over a prediction horizon $H \in \{24, 48\}$h, as proposed in this study. In response, the RNN models were trained using the root mean squared error as the loss function and optimized with the Adam optimizer (Section 3.4). The forecasting was separately conducted for the 24-h and 48-h surplus scenarios defined in Equations (4) and (5). This allows for the evaluation of RNN performance in capturing both very short-term and short-term temporal energy generation trends. Accurate forecasting of surplus energy at the micro-residential, community scale supports smarter control strategies for energy management and EV charging schedule regulation, contributing to more resilient, low-carbon community energy systems.

3.3.2. Long Short-Term Memory

The long short-term memory (LSTM) network, a specialized variant of recurrent neural networks, is designed to overcome the vanishing and exploding gradient problems that standard RNNs encounter when modeling long-term dependencies. This feature makes LSTM particularly effective for processing sequential data in community-scale building applications, where information from earlier time steps is crucial for interpreting the current and future trends. The architecture of LSTM includes a sophisticated system of memory and gating mechanisms (storage gates), which are an essential component of the model. Within the LSTM architecture, the storage gates are leveraged with hyperbolic tangent and sigmoid activation functions to effectively regulate the flow of information. The sigmoid-activation-function plays a crucial role in regulating the LSTM gates by setting the range of any given input along the x-axis to be between 0 and 1. This scaling guides the model in deciding how much past information should be retained or discarded as new sequential data comes in. In contrast, the hyperbolic tangent function transforms inputs into outputs within the range of -1 to 1. This ability allows the network to fine-tune the flow of information within the LSTM unit, thereby helping the model capture long-term dependencies more effectively.

The storage gates are central to the long short-term memory network's ability to retain information from earlier points in the sequence and apply it to future predictions, helping to overcome the memory limitations often found in simpler models. Specifically, the structure of each LSTM unit, as illustrated in Figure A2b in Appendix A, comprises a cell state C_t and three main gates—the input gate, the forget gate, and the output gate—that regulate the flow of information. The internal operations of an LSTM cell at time step t are given as follows:

$$f_t = \sigma\left(W_f \cdot [h_{t-1}, x_t] + b_f\right) \quad \{Forget\ gate\} \tag{10}$$

$$i_t = \sigma(W_i \cdot [h_{t-1}, x_t] + b_i) \quad \{Input\ gate\} \tag{11}$$

$$\widetilde{C}_t = tanh(W_c \cdot [h_{t-1}, x_t] + b_c) \quad \{Candidate\ cell\ state\} \tag{12}$$

$$C_t = f_t \odot C_{t-1} + t_i \odot \widetilde{C}_t \quad \{Cell\ state\ update\} \tag{13}$$

$$O_t = \sigma(W_o \cdot [h_{t-1}, x_t] + b_o) \quad \{Output\ gate\} \tag{14}$$

$$h_t = \hat{y}_t = O_t \odot tanh(C_t) \quad \{Hidden\ state\} \tag{15}$$

where f_t, i_t, O_t, and C_t represent the forget gate, input gate, output gate, and updated cell state, respectively. σ and $\odot$ donate the sigmoid activation function and element-wise multiplication, resp ectively. W_f, W_i, W_C, W_o and b_f, b_i, b_C, b_o are the trainable weights and biases. The forget gate determines which information from the cell state should be

discarded, while the input gate governs what new information is incorporated into the cell state. The output gate, then, decides which information should be output at the current time step. This configuration enables the LSTM to effectively handle both short-term and long-term dependencies, allowing it to retain and leverage pertinent information over extended time horizons.

Simultaneously, the newly updated short-term memory resulting from this inclusive process is what determines the output-gate. Within this-system-of-storage-gates, h_t and h_{t-1} represent the current and previous short-term memory outputs, while C_t and C_{t-1} indicate the corresponding long-term memory states, i.e., the present and the past. The input at each time step t is denoted as x_t. By decoupling the pathways for short-term and long-term memories, the LSTM network effectively mitigates the problems of exploding and vanishing gradients. The coordination of the forget, input, and output gates allows the LSTM model to selectively retain, update, or discard information, enabling more efficient handling of sequential data. This mechanism enhances the model's ability to perform forecasting tasks that involve time-dependent patterns.

3.3.3. Bidirectional Long Short-Term Memory

To further enhance the temporal learning capabilities of recurrent models, the BiLSTM network has introduced as a powerful method for sequence processing. Unlike standard LSTMs, which process input sequences unidirectionally (in a single forward direction from past to future), a BiLSTM propagates the input data in both forward and backward directions simultaneously [55], following Equations (16)–(18). This bidirectional structure enables the model to capture contextual dependencies from both past and future time steps, significantly improving its ability to learn complex temporal patterns in surplus energy dynamics influenced by cyclic behavior, such as daily solar generation and usage trends.

$$\overrightarrow{h_t} = LSTM_{forward}(x_t, \overrightarrow{h_{t-1}}) \tag{16}$$

$$\overleftarrow{h_t} = LSTM_{backward}(x_t, \overleftarrow{h_{t-1}}) \tag{17}$$

$$h_t^{(forward,\ \ backward)} = \phi\ [\overrightarrow{h_t}; \overleftarrow{h_t}] \tag{18}$$

As outlined in Equations (16) and (17), the BiLSTM network extracts features related to surplus energy load in both temporal directions, explicitly accounting for the complex time-dependent characteristics of the time series data. Each directional layer (forward and backward) employs its own activation function σ, and maintains independent hidden states: (a) the forward layer ($\overrightarrow{h_t}$) processes the sequence chronologically, capturing historical dependences, and (b) the backward layer ($\overleftarrow{h_t}$) processes the sequence in reverse, encoding future-contextual information. The final output $h_t^{(forward,backward)}$ of the BiLSTM is generated by integrating these directional states, as defined in Equation (18), where ϕ denotes a fusion operation (typically concatenation or summation). This dual-pathway structure ensures robust feature extraction for forecasting tasks where both past trends and future expectations influence predictions. Figure A3a in Appendix A illustrates a typical BiLSTM unit, and further details concerning hyperparameter optimization and model development are provided in Sections 3.4 and 3.6.

3.3.4. Gated Recurrent Units

While standard RNNs can effectively capture temporal dependencies in sequential data, they encounter significant challenges when dealing with long-term dependencies due to gradient-related issues, such as vanishing and exploding gradients. These limitations motivated the development of more advanced architectures, beginning with the

introduction of LSTM networks [56], as discussed in Section 3.3.2. Although LSTMs have demonstrated strong performance in time-series forecasting tasks, their high computational complexity and large number of parameters often result in longer training times, particularly when applied to large datasets. To address these challenges, the GRU was proposed as a more efficient alternative to the LSTM, offering comparable predictive performance with a simplified architecture and faster convergence [57]. GRUs reduce structural complexity by merging the input and forget gates into a single update gate, and by combining the hidden and cell state into a unified state vector. This refinement results in fewer trainable parameters, which contributes to more efficient training while preserving the model's capacity to learn temporal patterns.

The update gate determines how much of the previous hidden state should be retained, while the reset gate controls how much past information to discard when incorporating new input. Through this gating mechanism, GRUs can selectively update or maintain internal states, making them particularly effective at modeling sequential data with varying temporal dependencies. In this context, the internal operations of a GRU model at each time step t are described by the following equations:

$$z_t = \sigma(W_z \cdot [h_{t-1}, x_t] + b_z) \quad \{Update\ gate\} \tag{19}$$

$$r_t = \sigma(W_r \cdot [h_{t-1}, x_t] + b_r) \quad \{Rest\ gate\} \tag{20}$$

$$\tilde{h}_t = tanh(W_h \cdot [r_t \odot h_{t-1}, x_t] + b_h) \quad \{Candidate\ hidden\ state\} \tag{21}$$

$$h_t = (1 - z_t) \odot h_{t-1} + z_t \odot \tilde{h}_t \quad \{Final\ hidden\ state\} \tag{22}$$

where z_t and r_t are, respectively, the update and rest gates at time t. h_{t-1}, h_t, and $\tilde{h}_t$ donate the previous hidden state, the updated hidden state, and the candidate activation (new information), respectively. The update gate z_t governs the retention of past memory h_{t-1}, while the rest gate r_t determines how much of that past state is considered when generating the new candidate activation $\tilde{h}_t$. Together, these gates allow GRUs to flexibly manage temporal information, adapting to different sequence lengths and dynamics.

In this study, the GRU model is applied to forecast surplus energy at the micro-housing community scale using multivariate time-series inputs, as explained in Section 3.5. Figure A3b in Appendix A illustrates the internal architecture of a typical GRU. Compared to LSTM and BiLSTM, GRU's simpler design leads to faster training and lower computational demand, making it particularly well-suited for near real-time forecasting scenarios in micro-residential communities. This efficiency is critical for enabling timely decision-making in scheduling the cycles of charging EVs and energy management.

3.4. Method for Hyperparameter Optimization

The effectiveness of any forecasting model substantially depends on the selection of its hyperparameter values. Given the black-box nature of RNN architectures, fine-tuning these hyperparameters is a critical step in training accurate models. Common strategies for determining optimal hyperparameters involve Bayesian optimization, grid search, random search, and manual tuning [58,59]. Among these strategies, the optimal hyperparameter values for each model were determined using the controlled-variable method, which combines empirical expertise with an iterative grid search. This methodology aligns with approaches described in [16,59,60].

The controlled-variable method is an optimization strategy that systematically refines hyperparameter selection through targeted, iterative adjustments to maximize model performance. Unlike random or manual tuning, this method isolates each hyperparameter θ_i

within a constrained search space Θ_i, while holding all other parameters $\theta_{\neg i}$ constant. For each candidate configuration $\theta_i^{(k)}$, the validation loss $\mathcal{L}_{val}\left(\theta_i^{(k)}, \theta_{\neg i}\right)$ is evaluated. The optimal value θ_i^* is then selected through minimization, as shown in Equations (23) and (24).

$$\Theta_i = \left\{\theta_i^{(1)}, \theta_i^{(2)}, \ldots, \theta_i^{(N)}\right\}, \theta_i^{(k)} \in \left[\theta_i^{min}, \theta_i^{max}\right] \tag{23}$$

$$\theta_i^* = \underset{\theta_i \in \Theta_i}{argmin} \mathcal{L}_{val}(\theta_i, \theta_{\neg i}) \tag{24}$$

The process terminates when the change in validation loss between successive iterations stratifies the convergence condition $\left|\mathcal{L}_{val}^{(t+1)} - \mathcal{L}_{val}^{(t)}\right| < \epsilon$. This ensures precision comparable to a full grid search, while significantly reducing redundancy in the parameter space. The optimization procedure iteratively adjusts hyperparameter values to enhance performance, continuing until the best set of parameters (optimal configuration) is identified. For implementation, Python's GridSearchCV algorithm was used to carry out the controlled-variable method through constrained, sequential evaluation of predefined parameter combinations. GridSearchCV proved to be both an efficient and flexible technique for identifying optimal hyperparameter configurations [59,61]. This study predefined a range of values for each target hyperparameter and incorporated random seeds into the optimization process to ensure consistent convergence and reduce variability. The specific hyperparameters and their search ranges are summarized in Table 3. For the RNN model, two stacked recurrent layers with 32–64 neurons per layer, dropout rate 0.1, and batch size 96–128 were used, with the Adam optimizer and ReLU activation. The LSTM model employed 2–3 stacked layers with 64 neurons per layer, dropout 0.1, batch size 32–64, Adam optimizer, and ReLU activation. The BiLSTM model used two stacked layers with 32–64 neurons, dropout 0.1, batch size 64–96, Adam optimizer, and ReLU activation. The GRU model consisted of 2–3 stacked layers with 64 neurons, dropout 0.1, batch size 64, Adam optimizer, and ReLU activation. These configurations were selected through the controlled-variable method to optimize forecasting performance across all seasonal datasets.

Table 3. Hyperparameter optimization search range for RNN architecture-based forecasting models.

Model	Hyperparameter	Search Space/Range	Optimal Selected Value
RNN	RNN sequence	[12, 24, 32, 64]	[32, 64]
	Epochs	[50, 100, 200, 600]	[200, 600]
	Stacked layers	[1, 2, 3, 4]	[2]
	Optimization function (optimizer)	Adam, nadam	Adam
	Activation function in RNN cells	relu, sigmoid, tanh	Relu
	Batch size	[32, 64, 96, 128]	[96, 128]
	Dropout rate	[0.1, 0.2, 0.3, 0.4]	[0.1]
	Learning are	[0.001, 0.01, 0.1, 0.02]	[0.01]
LSTM	LSTM sequence	[24, 32, 64, 96]	[64]
	Epochs	[50, 100, 200, 400]	[200, 400]
	Stacked layers	[2, 3, 4, 5]	[2, 3]
	Optimization function (optimizer)	Adam, nadam	Adam
	Activation function in LSTM cells	relu, sigmoid, tanh	Relu
	Batch size	[16, 32, 64, 96]	[32, 64]
	Dropout rate	[0.1, 0.2, 0.3, 0.4]	[0.1]
	Learning rate for optimizer	[0.0001, 0.001, 0.05, 0.01]	[0.01, 0.001]

Table 3. *Cont.*

Model	Hyperparameter	Search Space/Range	Optimal Selected Value
BiLSTM	BiLSTM sequence (Sequence-length)	[12, 18, 24, 64]	[32, 64]
	Epochs	[30, 50, 100, 200]	[100, 200]
	Stacked layers	[2, 3, 4, 5]	[2]
	Optimization function (optimizer)	Adam, nadam	Adam
	Activation function in BiLSTM cells	relu, sigmoid, tanh	Relu
	Batch size	[32, 64, 96, 128]	[64, 96]
	Dropout rate	[0.1, 0.2, 0.3, 0.4]	[0.1]
	Learning rate	[0.001, 0.01, 0.1, 0.03]	[0.01]
GRU	GRU sequence (Sequence-lengths)	[24, 48, 64, 96]	[64]
	Epochs	[150, 200, 400, 600]	[200, 400]
	Stacked layers	[2, 3, 5, 6]	[2, 3]
	Optimization function (optimizer)	Adam, nadam	Adam
	Activation function in GRU cells	relu, sigmoid, tanh	Relu
	Batch size	[32, 64, 96, 128]	[64]
	Dropout rate	[0.1, 0.2, 0.3, 0.4]	[0.1]
	Learning rate	[0.0001, 0.001, 0.01, 0.1]	[0.01]

3.5. Data Preprocessing and Input Selection Method

Accurately forecasting surplus energy availability at the micro-residential community level is a complex task due to the multiple factors influencing onsite energy generation and the varying energy demands of the community's residents. To address this challenge, this study employed Pearson correlation coefficients (PCCs), which were chosen for their low computational cost [62], to understand how the future surplus energy correlates with these influencing factors. PCC takes values between (+1) and (−1), where higher absolute values of PCCs translate to an input variable closely related to the availability of future surplus energy. Specifically, a positive PCC value implies that higher values of one input variable are generally associated with higher values of the other variable. For instance, increased surplus energy may often occur in conjunction with greater solar radiation. A negative PCC value would indicate that higher values of one input variable are typically associated with lower values of the other (e.g., decreased surplus energy may often occur as a result of rising ambient temperature).

Using the PCC approach, the input variables to the forecasting models were carefully selected based on their correlation level with potential future community-scale surplus energy. The chosen input variables in this study include outdoor air temperature (Temp), relative humidity (RH), wind speed (WS), horizontal global solar irradiance (HGSI), diffuse solar radiation (DSR), direct normal solar intensity (DNSI), hour of the day (hour), and day of the week (DayWeek). These variables are essential for accurately forecasting the availability of onsite surplus energy at the community level and can be readily obtained from local weather data sources [63,64]. Following a thorough correlation analysis, these selected hourly time-series data values formed the basis for developing baseline models based on RNN architectures. This method guarantees that all models are grounded in realistic environmental conditions, thereby improving their forecasting accuracy and practical relevance for surplus energy prediction tasks. Including household demand as an input feature could potentially improve short-term surplus energy forecasting accuracy, particularly during periods of high load variability or atypical consumption patterns. This would be especially important in cases where detailed load scheduling or individual household behavior significantly affects community-level surplus energy.

Figure 7 illustrates the correlations between the selected input variables and surplus energy availability. Horizontal global solar irradiance, diffuse solar radiation, and direct

normal solar intensity exhibit strong correlations with future surplus energy. However, advanced deep learning models are capable of extracting valuable information patterns even from input variables with low PCC values [65]. Because these models can capture complex nonlinear relationships, including variables with lower linear correlation values, they ensure that higher-order correlations are not overlooked during model training. The input variable selection process was conducted independently of the forecasting models, and the same set of input variables was used for each model and forecast horizon. As for data preprocessing, the dataset was not standardized, and no mean removal or variance scaling was applied to the input features, as all variables are expressed in consistent units (kWh for energy, standard SI units for weather parameters) with similar numerical ranges. This allows the RNN, LSTM, BiLSTM, and GRU models to learn meaningful patterns directly from the raw data.

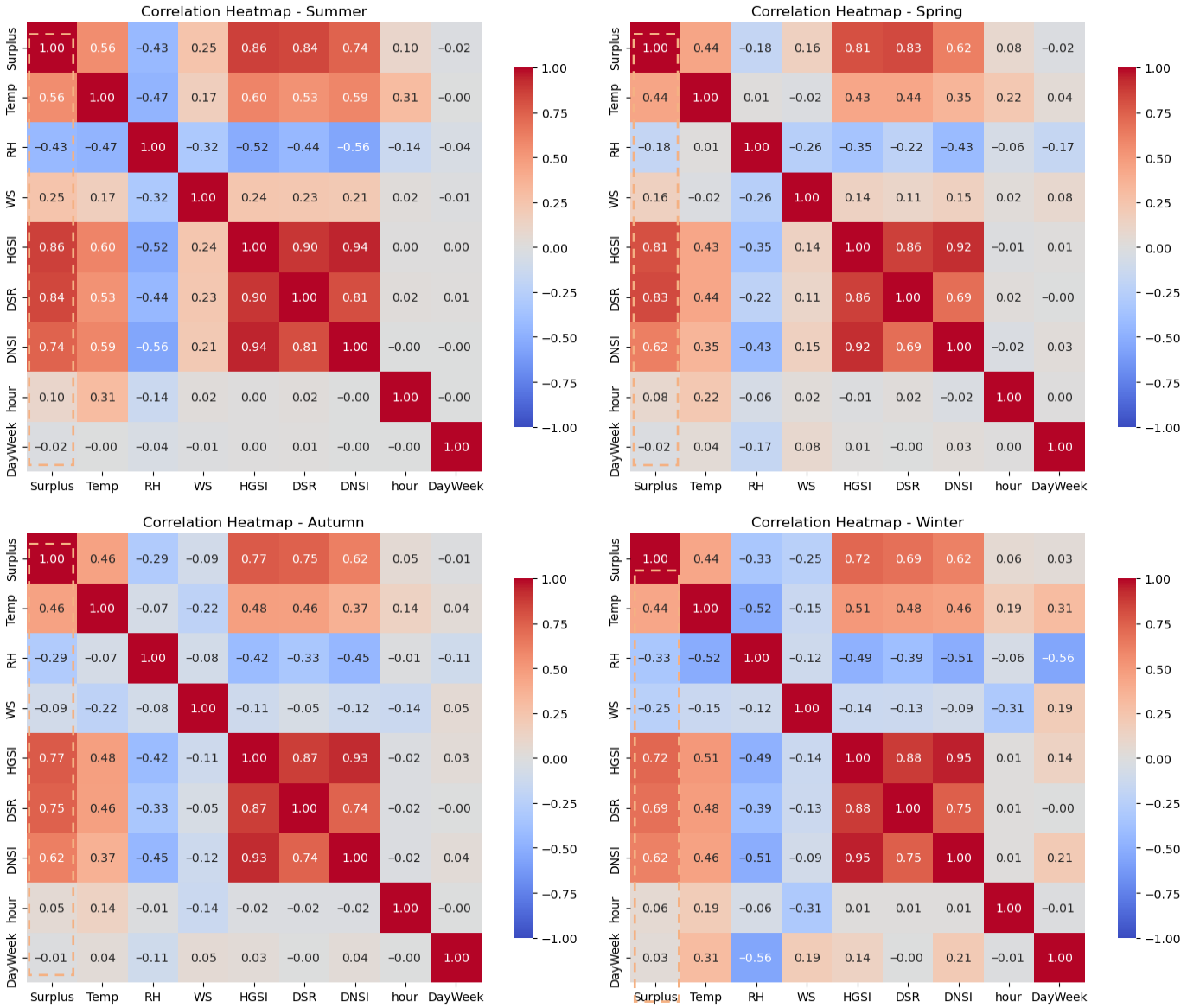


Figure 7. Correlation heatmaps of input variables in relation to surplus energy availability for each period.

3.6. Forecast Framework Development

This section describes how the RNN, LSTM, BiLSTM, and GRU models were developed and implemented for surplus energy forecasting at the micro-residential community

level. Data-driven approaches to predict the future surplus energy require a thorough input dataset comprising a variety of influential variables. While multiple factors can influence the availability of surplus energy, this study categorized the input variables into three main groups [64]: time-related features, past energy demand, and environmental variables. Since environmental variables are primarily driven by outdoor weather conditions, the study considered horizontal global solar irradiance, diffuse solar radiation, direct normal solar intensity, wind speed, relative humidity, and outdoor air temperature, readily available from open local-weather-forecast sources, as a core part of the input dataset. Further, time-related features incorporated into the input dataset included hour of the day and day of the week, dataset duration, and seasonal categorizations. A correlation analysis was conducted to assess the relationship between surplus energy availability and the selected input variables under distinct seasonal conditions, as described in Section 3.5. This step was critical for capturing the temporal and seasonal production patterns of distributed rooftop PV systems, which are significantly shaped by fluctuations in both weather and residential energy usage. It is also important to note that while past household energy demand is recognized as a key driver of surplus energy availability, it was deliberately excluded from the forecasting models in this study. This is primarily due to the significant logistical challenges associated with acquiring real-world household energy data, including measurement permissions and occupant privacy concerns. Instead, a PV-centric forecasting approach was adopted, as surplus availability is primarily constrained by generation patterns rather than consumption behaviors in the studied context.

Figures A2 and A3 in Appendix A illustrate the detailed architecture of each developed model, outlining the setup of their input, hidden, and output layers. Each architecture is designed to capture nonlinear relationships and temporal dependencies between the input variables. The input layer receives the multivariate time-series features selected during the input preparation phase, while the hidden layers are constructed using recurrent units specific to each model type. The model design process began with an initial optimization phase aimed at identifying the optimal number of layers and neurons, testing configurations that included up to five stacked layers for each RNN, LSTM, BiLSTM, and GRU architecture. The number of neurons was gradually reduced across layers to enable progressive feature extraction and refinement. Each model ends with a fully connected output layer, a final single dense neural layer, responsible for predicting surplus energy values. The chosen input variables included the horizontal global solar irradiance, diffuse solar radiation, direct normal solar intensity, wind speed, relative humidity, outdoor air temperature, and surplus energy data. Those variables were selected for their strong impact on prediction accuracy and their availability from local data sources. To prevent information leakage in the time-series forecasting task, the dataset was split strictly in chronological order, with earlier observations used for training, followed by validation, and the most recent data reserved for testing.

To implement these stacked models, this study employed several Python libraries, primarily TensorFlow and Scikit-learn, which provided the essential tools for building, training, and evaluating the models. Furthermore, Pandas was used for dataset manipulation and organization within data frames, NumPy for efficient numerical operations, and Matplotlib for visualizing results. This combination of tools supported a robust and efficient workflow for managing and analyzing time-series datasets. Table 3 presents representative examples of the key hyperparameters optimized during the initial model development phase for surplus energy forecasting. These hyperparameters were identified through the controlled-variable optimization method described in Section 3.4. Each model was trained on 70% of the annual simulated dataset, while the remaining 30% was used for testing and validation to predict future surplus energy availability. To prevent

information leakage in the time-series forecasting task, the dataset was split strictly in chronological order, with the first 70% of the annual data used for training and the last 30% reserved for testing and validation. The models learned temporal dependencies in the multivariate time-series data composing the preselected environmental and temporal input variables for 24-h and 48-h forecast horizons. All models were trained using the mean squared error loss function, which penalizes larger deviations more strongly and is well-suited for regression-based surplus energy forecasting. To mitigate overfitting, given the relatively small dataset, regularization techniques, including dropout layers within the hidden recurrent units and early stopping during training, were applied, ensuring that the models generalize effectively while capturing meaningful temporal dependencies. In addition to surplus energy forecasting, the same RNN-based models were independently applied to forecast baseline energy demand and onsite PV generation. This allowed for a comparative analysis and cross-validation of the predicted surplus energy. At each stage, model performance was evaluated using the evaluation metrics introduced in Section 3.7, ensuring a consistent and rigorous comparison across all forecasting tasks.

3.7. Performance Indices for Framework Assessment

To statistically evaluate the accuracy of each forecasting model and compare it with other common data-driven models, four primary performance indices were employed in this study. These included the mean absolute percentage error (MAPE), root mean square error (RMSE), mean absolute error (MAE), and the determination coefficient (R^2). These indices were selected due to their capacity to provide a comprehensive assessment of model performance in terms of both forecasting accuracy and alignment with actual observed data [53,66]. The trained models were applied to predict the hourly surplus energy availability, as well as the baseline energy demand and onsite energy generation, using the test dataset. The forecasted values produced by each model were then compared to the corresponding actual (simulated) values. MAPE, RMSE, MAE, and R^2 were computed based on the following Equations (25)–(28).

$$MAPE = \left(\frac{1}{n} \sum_{i=1}^{n} \left| \frac{y_{actual,i} - \hat{y}_{forecast,i}}{y_{actual,i}} \right| \right) \times 100 \quad (25)$$

$$RMSE = \sqrt{\frac{1}{n} \sum_{i=1}^{n} \left(y_{actual,i} - \hat{y}_{forecast,i} \right)^2} \quad (26)$$

$$MAE = \frac{1}{n} \sum_{i=1}^{n} \left| y_{actual,i} - \hat{y}_{forecast,i} \right| \quad (27)$$

$$R^2 = 1 - \frac{\sum_{i=1}^{n} \left(y_{actual,i} - \hat{y}_{forecast,i} \right)^2}{\sum_{i=1}^{n} \left(y_{actual,i} - \overline{y} \right)^2} \quad (28)$$

where $\hat{y}_{forecast,i}$ is the forecasted value of the model at hour i, $y_{actual,i}$, is the corresponding actual (simulated) value at hour i, $\overline{y}$ is the mean of the actual values, and n is the total number of observations. MAPE measures the average percentage error between forecasted and actual values, offering an intuitive interpretation of forecasting accuracy. RMSE reflects the standard deviation of the residuals (forecast errors), indicating how closely the forecasts cluster around the actual values. MAE calculates the average absolute difference between forecasted and actual values, serving as a direct measure of error magnitude, and R^2 represents the proportion of variance in the actual surplus energy that is explained by the model, serving as an indicator of model fit. In this study, MAPE was adopted as the primary performance indicator due to its interpretability and sensitivity to relative error. MAE, RMSE, and R^2 were used as secondary criteria (tie breakers) to distinguish between models when MAPE alone did not show a significant difference among model performances.

Generally, lower values of MAPE, RMSE, and MAE indicate better forecasting accuracy, reflecting the capacity of the model in reducing the gap between forecasted and actual values. For R^2, values range from 0 to 1; values closer to 1 indicate a better fit, indicating that the model accounts for a larger proportion of the observed variance in surplus energy availability. In this study, all performance metrics were evaluated on the test set of the dataset to provide an unbiased assessment of the models' generalization capability on unseen data.

4. Results and Discussion

This section presents the results of implementing RNN architecture-based models to forecast surplus energy availability at the micro-residential community level. It first evaluates the effectiveness of implementing base RNN models for forecasting baseline household energy demand and onsite generation, analyzing their performance, and establishing benchmark models for subsequent comparison. The evaluation then shifts to the primary forecasting tasks: predicting community-scale surplus energy availability. The performance of multiple RNN-based models, namely RNN, LSTM, BiLSTM, and GRU, is assessed across different seasons: summer, spring, autumn, and winter. This seasonal breakdown enables a detailed understanding of how each model handles the variability introduced by climate and solar patterns throughout the year. Furthermore, the performance of these models is compared with other commonly used data-driven models, providing a comprehensive benchmark. This comparative evaluation aims to determine how well each model improves forecasting accuracy by minimizing the discrepancy between predicted and actual surplus energy values. Lastly, the use of these models' forecasted values to manage EV charging schedules is discussed.

4.1. Baseline Models for Forecasting Demand and Onsite Generation

4.1.1. 24-h-Ahead Forecast Models

Figure 8 presents a visual comparison between the forecasted and actual values of energy demand and onsite energy generation for the micro-residential community during a representative period of the year. Specifically, it visually contrasts the 24-h-ahead forecasts produced by the RNN, LSTM, BiLSTM, and GRU models against the simulated ground-truth ("Actual") values for both energy demand and onsite PV generation. The developed baseline models were trained and evaluated using 12-month datasets covering both community-scale energy demand and onsite generation. Specifically, 70% of the dataset was used for training. To avoid inducing a bias in the performance outcomes, 20% of the remaining dataset was set aside to test the model, and the final 10% was used as a validation dataset to assess the performance of trained models during the forecasting phase. This data partitioning strategy aligns with common recommendations in AI-based, data-driven modeling practices [62,67]. For onsite generation forecasting, the models utilized input features identified through the PCC analysis to predict future generation profiles between 8:00 AM and 6:00 PM over a 24-h horizon. Similarly, the same set of input features was used to forecast energy demand profiles spanning from 0:00 AM to 23:00 PM within the same horizon.

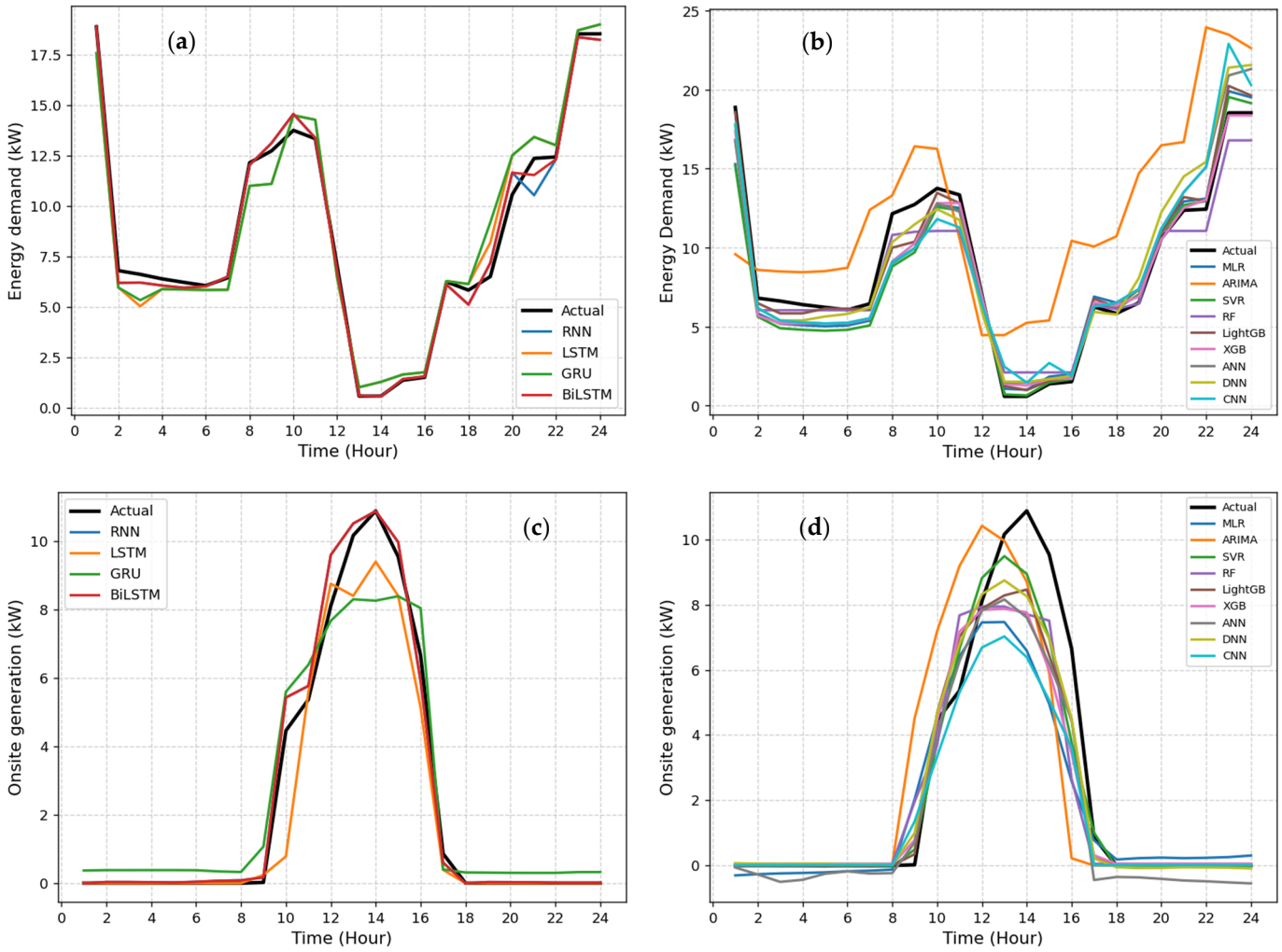


Figure 8. Representative comparison of forecasting patterns for energy demand and onsite energy generation over a 24-h-ahead horizon.

Table 4 presents the statistical results for energy demand and onsite energy generation forecasts, including forecasting accuracy over a 24-h-ahead horizon. The results in this table demonstrate that the RNN, BiLSTM, GRU, and LSTM models perform well in forecasting tasks. The estimated MAPE values for energy demand forecasts, as shown in the table, are 7.38%, 8.29%, 9.12%, and 10.38%, respectively. Similarly, onsite energy generation forecasts capture accurate values of 11.14%, 11.49%, 15.01%, and 16.39%. The R^2 values for energy demand and onsite energy generation forecasts range from 0.960 to 0.936, and from 0.789 to 0.718, respectively. These high R^2 values indicate a strong fit, suggesting that the models could explain a large proportion of the observed variance in both energy demand and onsite energy generation. The RMSE and MAE values for hourly energy demand and onsite energy demand forecasts were within acceptable ranges, not exceeding 1.85 kW and 1.63 kW, respectively. Notably, the demand energy forecasts showed higher accuracy in terms of RMSE and MAE. Among the evaluated models, the RNN, followed by the BiLSTM, outperformed the GRU and LSTM models in providing accurate forecasts for both energy demand and onsite energy generation. This highlights the capability of models trained on adequate datasets to accurately capture energy demand and onsite generation trends over the next 24 h, resulting in highly accurate forecasting outputs.

Table 4. Performance results of baseline RNN-based models compared to common data-driven models over a 24-h horizon.

Model	Energy Demand				Onsite Generation			
	R^2	MAE	RMSE	MAPE	R^2	MAE	RMSE	MAPE
RNN	0.960	0.33	0.47	7.38	0.789	1.04	1.81	11.14
LSTM	0.936	0.43	0.65	10.38	0.768	1.04	1.79	15.01
BiLSTM	0.956	0.38	0.52	8.29	0.785	1.04	1.84	11.49
GRU	0.945	0.42	0.61	9.12	0.718	1.63	1.85	16.39
CNN	0.899	0.58	0.81	17.36	0.475	2.57	3.31	36.29
DNN	0.897	0.61	0.78	25.47	0.704	1.75	1.96	32.17
ANN	0.892	0.63	0.80	26.78	0.660	1.89	2.02	40.21
XGB	0.954	0.48	0.63	15.62	0.694	1.92	2.16	29.56
LightGB	0.961	0.52	0.68	11.68	0.679	1.95	2.05	25.28
RF	0.825	0.84	1.07	36.39	0.666	2.05	2.15	36.04
SVR	0.938	0.74	0.77	13.84	0.667	1.74	2.14	32.56
MLR	0.908	0.62	0.86	20.46	0.609	1.92	2.12	43.26
ARIMA	0.175	1.62	2.34	58.63	0.621	2.24	2.85	25.06

Compared to other common data-driven models, including CNN, DNN, ANN, XGB, RF, ARIMA, and MLR, the performance of RNN, BiLSTM, LSTM, and GRU models becomes even more evident in Figure 8, where they demonstrate superior accuracy by reducing the gap between forecasted and actual values for both energy demand and onsite energy generation. For instance, the estimated MAPE values of the RF and ARIMA models were 36.39% and 58.63%, respectively, for energy demand forecasts. Similarly, the MAPE values for onsite energy generation forecasts were significantly higher for CNN (36.29%), ANN (40.21%), RF (36.04%), and MLR (43.26%), indicating lower accuracy. This performance gap can be attributed to two primary reasons. First, onsite generation from distributed rooftop PV systems is highly nonlinear and sensitive to outdoor weather fluctuations, which linear models such as MLR cannot capture. Additionally, RF models often suffer from instability when dealing with sparse datasets [68], as is the case in this study. Second, traditional ANNs are limited in their ability to capture temporal dependencies, which are essential for time-series forecasting. These limitations highlight the superiority of RNN architecture-based models in delivering highly accurate 24-h-ahead predictions.

4.1.2. 48-h-Ahead Forecast Models

As regards the 48 h forecasts, Table 5 summarizes the MAPE, RMSE, MAE, and R2 values for each model in predicting energy demand and onsite energy generation, respectively. By comparing the forecasting performance for each model, it can be concluded that the 48-h-ahead forecasting models based on RNN, BiLSTM, LSTM, and GRU methods exhibit higher overall accuracy compared to their counterparts among other common data-driven models. All RNN, BiLSTM, LSTM, and GRU models achieved lower values of MAPE, RMSE, and MAE; and higher values of R^2, than those achieved by other models, including CNN, DNN, MLR, and ANN models. Similar to the 24-h-ahead predictions, the accuracy of each model varies depending on the AI algorithm employed and the intended forecasting horizon. Notably, the RNN model, followed by BiLSTM and LSTM, significantly reduced the magnitude of forecasting errors, with RMSE and MAE values not exceeding 2.52 kW and 1.43 kW, respectively, for both energy demand and onsite energy generation.

Table 5. Performance results of baseline RNN-based models compared to common data-driven models over a 48-h horizon.

Model	Energy Demand				Onsite Generation			
	R^2	MAE	RMSE	MAPE	R^2	MAE	RMSE	MAPE
RNN	0.958	0.35	0.75	7.38	0.878	1.33	1.97	9.51
LSTM	0.955	0.37	0.85	7.78	0.856	1.43	2.52	15.85
BiLSTM	0.956	0.36	0.74	7.48	0.876	1.35	1.84	9.49
GRU	0.934	0.49	0.96	14.39	0.835	1.82	2.58	15.39
CNN	0.708	0.89	1.36	22.06	0.707	3.02	3.83	26.06
DNN	0.892	0.61	1.13	25.04	0.802	1.78	4.86	32.65
ANN	0.888	0.63	1.11	25.77	0.813	1.94	4.95	38.01
XGB	0.924	0.53	0.99	15.63	0.798	1.95	2.82	30.17
LightGB	0.929	0.51	0.99	15.75	0.789	1.96	2.89	26.03
RF	0.825	0.85	1.08	36.40	0.783	1.83	2.87	36.56
SVR	0.917	0.64	1.07	16.98	0.798	1.98	2.67	33.14
MLR	0.909	0.62	2.65	20.38	0.798	1.93	2.85	43.82
ARIMA	0.052	1.94	1.75	74.08	0.698	2.01	2.99	24.08

Figure 9 provides a comparison visualization of forecasted versus actual energy demand and onsite energy generation patterns over a 48-h horizon. As shown in Figure 9a,c, the RNN, LSTM, BiLSTM, and GRU models consistently follow the general pattern of both energy demand and onsite energy generation, with effective periodic fluctuations and rapid transitions. Notably, BiLSTM and RNN exhibit superior performance, maintaining close to alignment with actual values during high-demand peaks around hours 12, 22, and 25 (Figure 9a). GRU and LSTIM also demonstrate strong tracking ability, with slight deviations during sharp transitions. In contrast, Figure 9b,d reveals that the other models, such as MLR, ARIMA, SVR, LightGB, XGB, ANN, DNN, and CNN, struggle to accurately predict the general pattern of both energy demand and onsite energy generation.

Meanwhile, ARIMA notably smooths out sharp variations, failing to capture significant peaks and valleys, while MLR and RF models frequently underpredict demand during critical intervals, as illustrated in Figure 9b,d. ANN, DNN, and CNN also exhibit inconsistent performance, particularly during transitional phases, reflecting their limitations in accurately modeling complex temporal dependencies. In contrast, the RNN, BiLSTM, LSTM, and GRU models successfully replicate the expected onsite generation profile, which is characterized by pronounced solar output peaks around hours 16 and 40 and zero-generation periods during nighttime. Among them, BiLSTM achieves the closest alignment with actual values during peak generation, followed by RNN, while GRU and LSTM slightly underpredict during high-insolation intervals yet still preserve the overall trend. These visual patterns reinforce the quantitative performance metrics reported in Table 5, further confirming that RNN architecture-based models outperform traditional models in capturing both temporal dynamics and nonlinear behaviors in energy demand and onsite energy generation. This promotes the adoption of these models as reliable candidates for forecasting surplus energy availability in micro-residential communities, as discussed in Section 4.2.

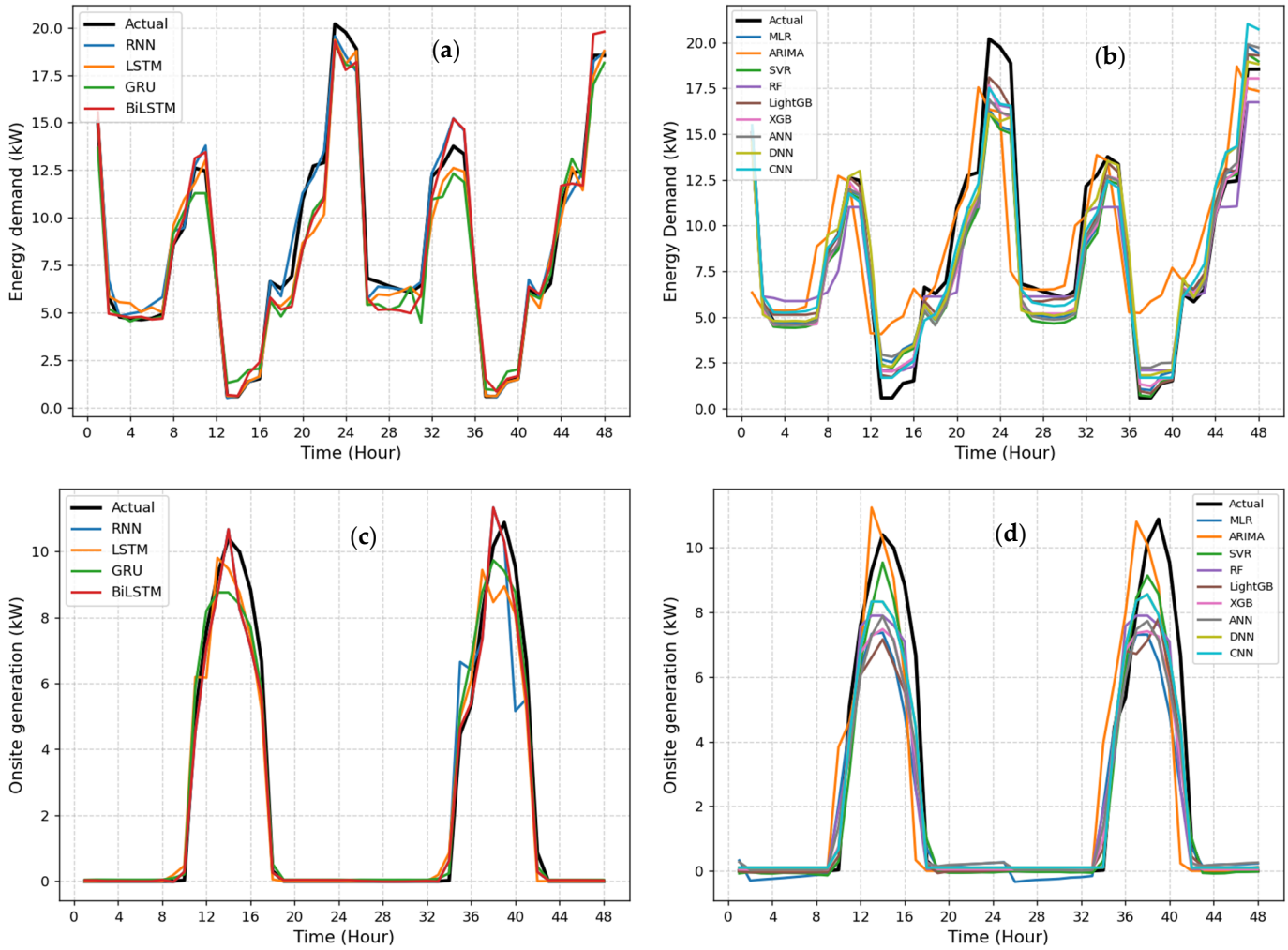


Figure 9. Representative comparison of forecasting patterns for energy demand and onsite energy generation over a 48-h-ahead horizon.

4.2. Forecasting Models for Surplus Energy Availability

4.2.1. Surplus Forecast Models for the 24 h/24 h Scenario

This section provides a comparative analysis of forecasting surplus energy availability at the micro-residential community level, focusing on the first scenario, which assumes the potential for onsite energy generation and demand over 24 h, as defined by Equation (4). Figures 10–13 illustrate the comparative results for forecasting short-term surplus energy availability by highlighting the seasonal influence on the forecasting model performance. All models were trained and evaluated using hourly datasets for each season: winter (22 December to 21 March), spring (22 March to 20 June), summer (21 June to 22 September), and autumn (22 September to 21 December). The same input features identified through the PCC analysis were used (as in the baseline models) to predict the potential surplus energy profile between 8:00 AM and 6:00 PM over both 24-h- and 48-h-ahead horizons. This approach enables comprehensive predictions of surplus energy and facilitates the evaluation of each proposed model's effectiveness in providing accurate estimates of potential availability during the specified daytime interval.

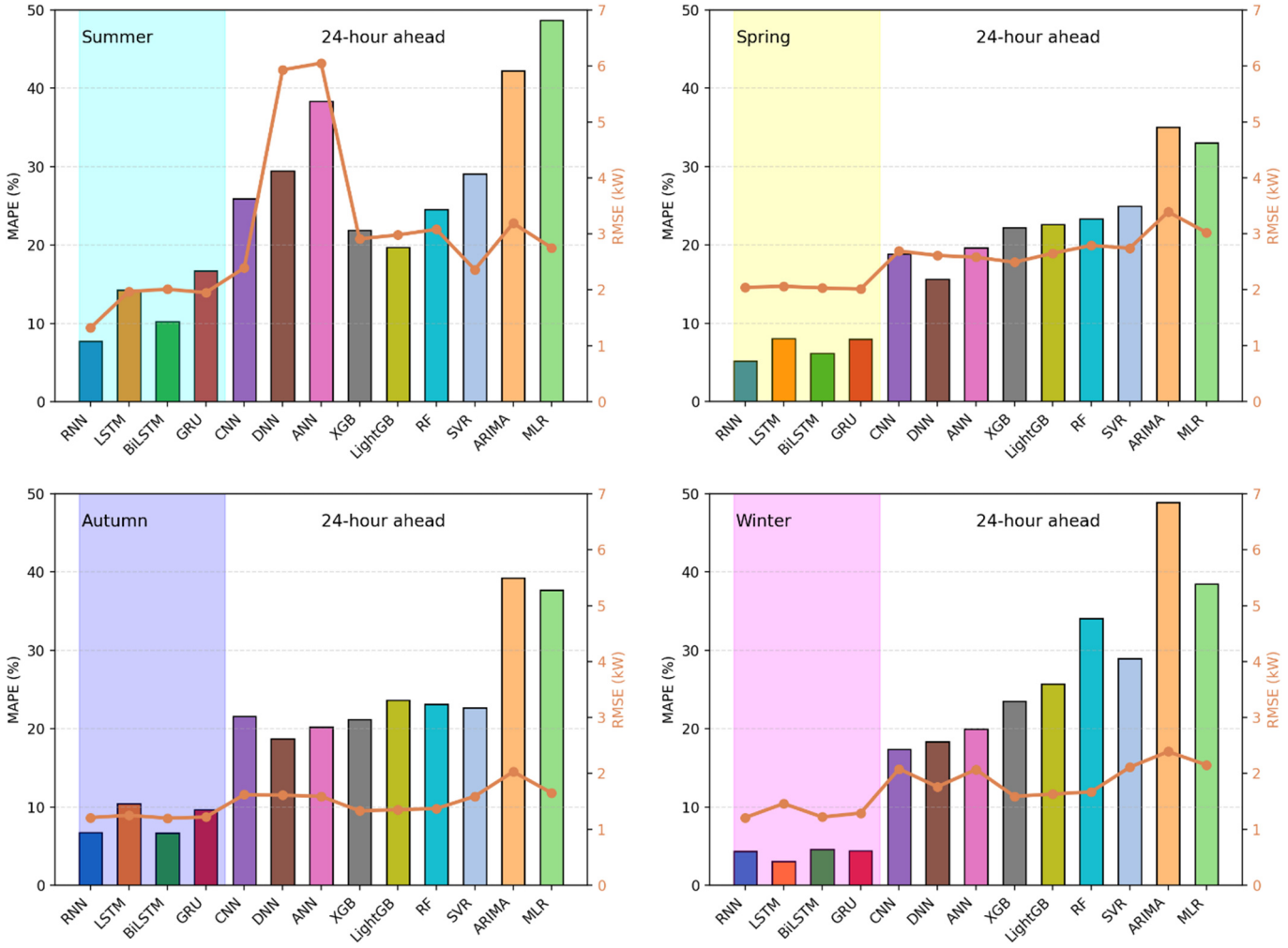


Figure 10. Comparison of MAPE and RMSE values for various RNN-based models and their counterparts of common data-driven models in forecasting energy surplus under the first scenario over a 24-h-ahead horizon.

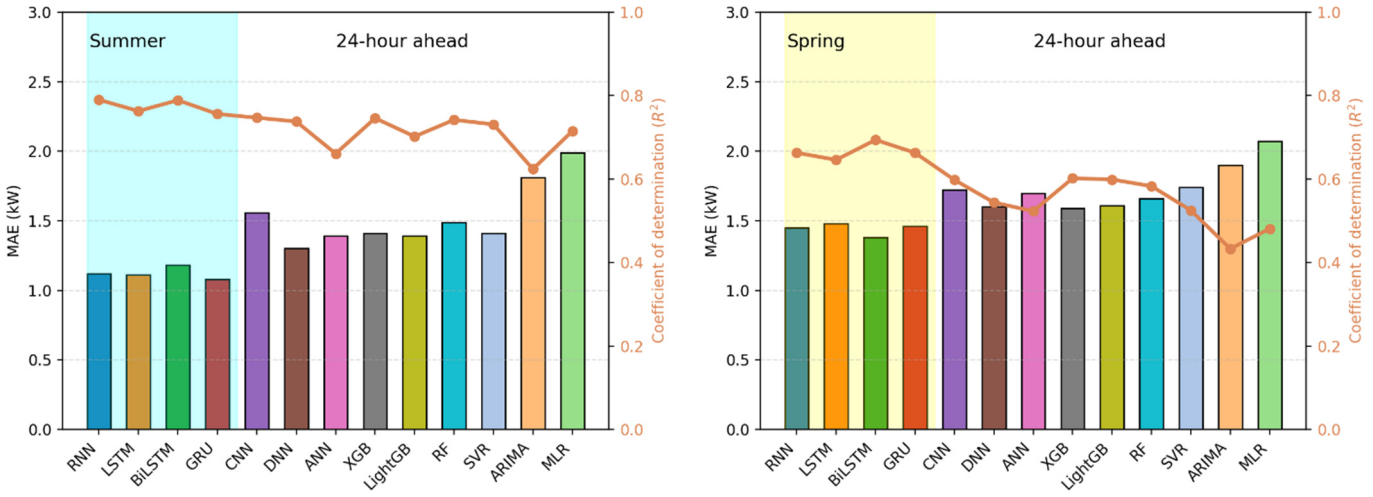


Figure 11. *Cont.*

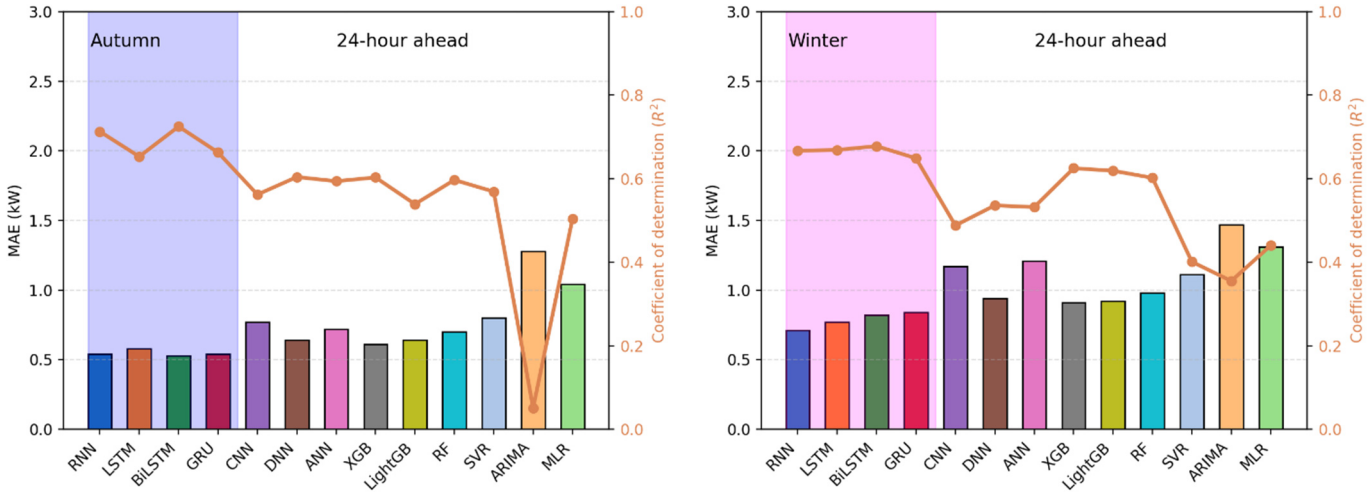


Figure 11. Comparison of MAE and R^2 values for various RNN-based models and their counterparts of common data-driven models in forecasting energy surplus under the first scenario over a 24-h-ahead horizon.

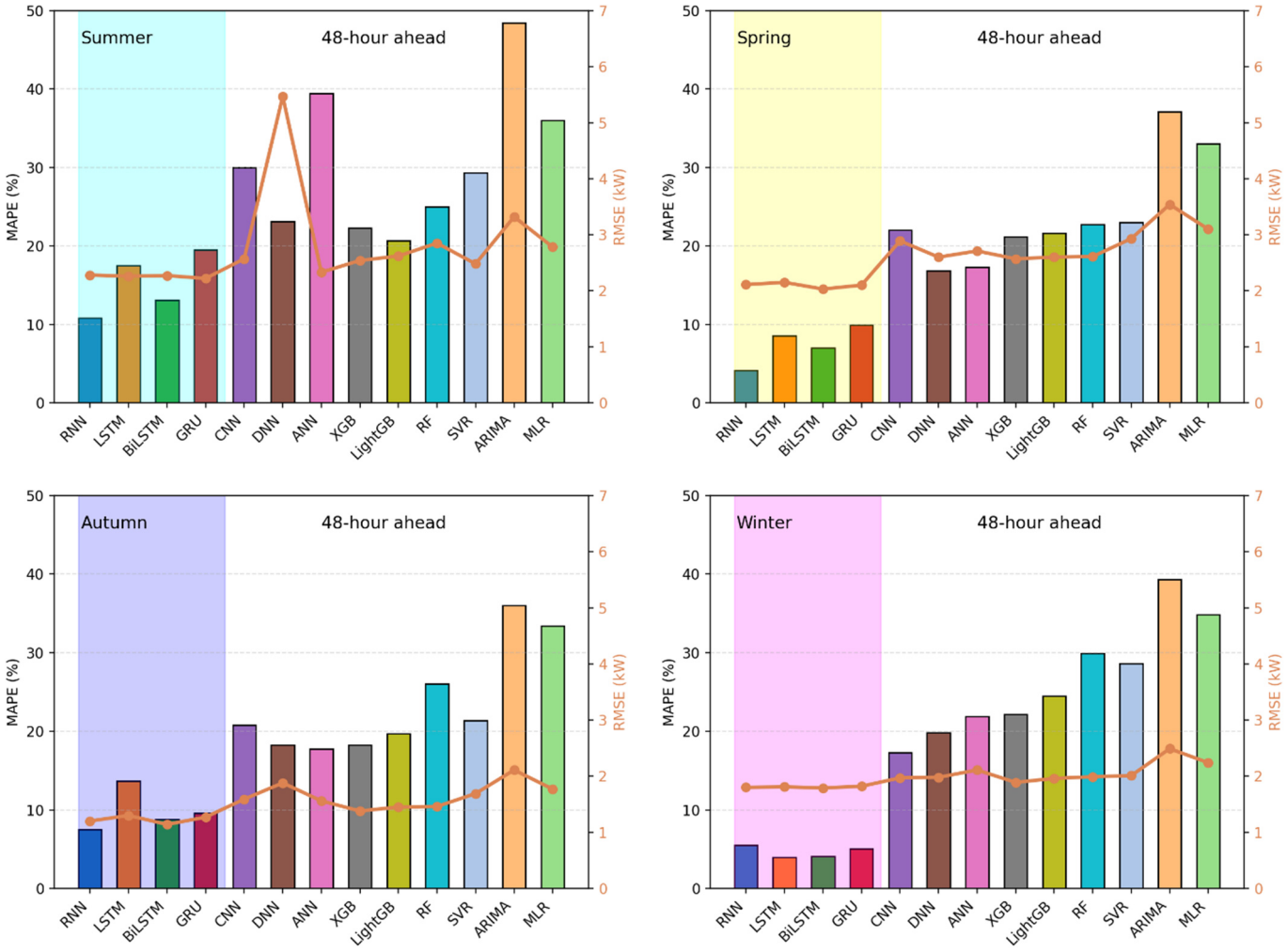


Figure 12. Comparison of MAPE and RMSE values for various RNN-based models and their counterparts of common data-driven models in forecasting energy surplus under the first scenario over a 48-h-ahead horizon.

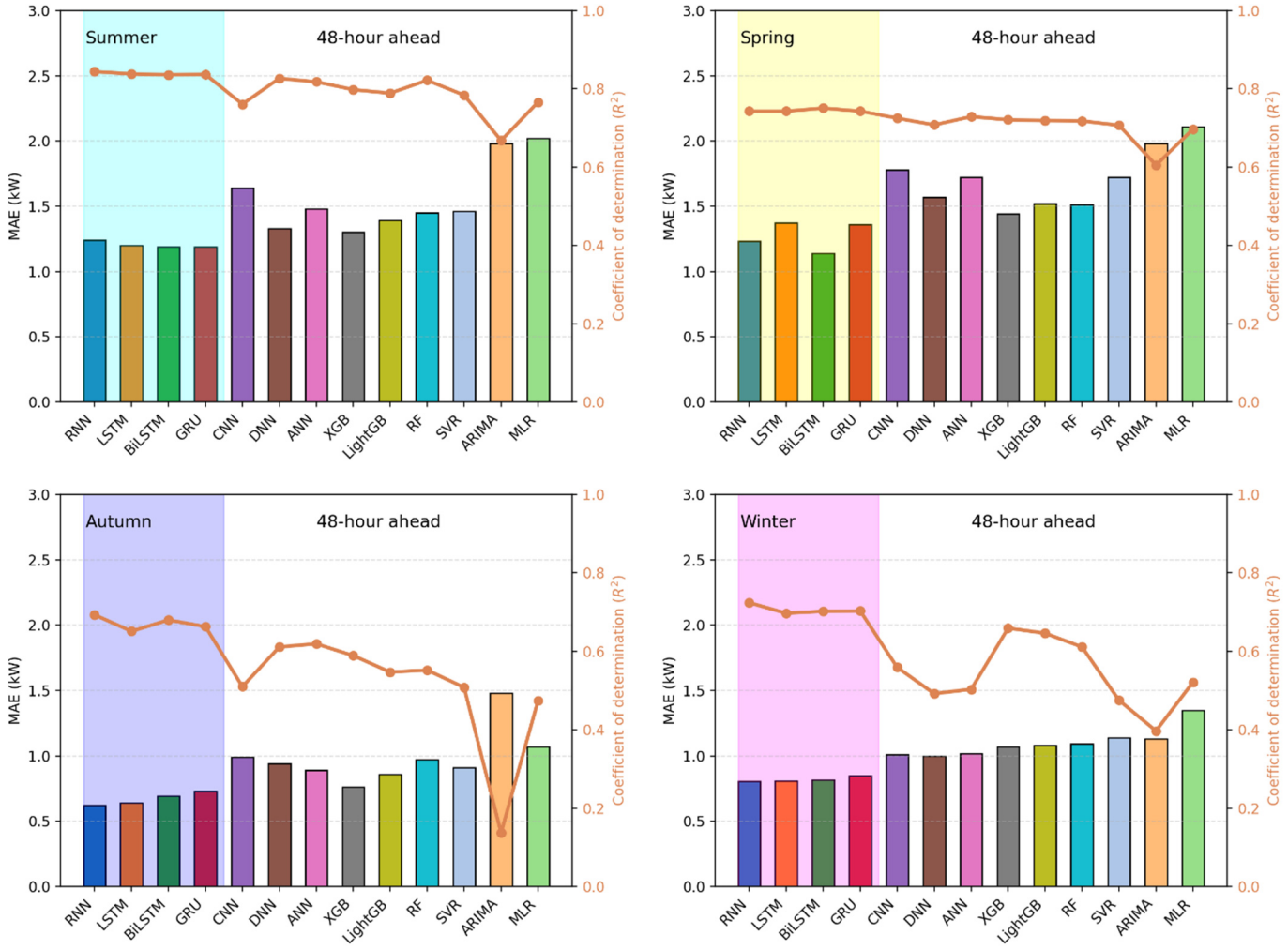


Figure 13. Comparison of MAE and R^2 values for various RNN-based models and their counterparts of common data-driven models in forecasting energy surplus under the first scenario over a 48-h-ahead horizon.

Figures 10 and 11 provide a comparative analysis of the forecasting performance of RNN, BiLSTM, LSTM, and GRU models compared with other models, in terms of MAPE, RMSE, MAE, and R2 at a 24-h-ahead horizon across different seasons: summer, spring, autumn, and winter. As shown in Figure 10, RNN-based models, particularly BiLSTM and RNN, consistently outperform traditional models, such as MLR, SVR, RF, and ANN. Both RNN and BiLSTM achieved the most accurate forecasts of energy surplus, especially in capturing the peak and valley patterns of surplus availability, as reflected by their lower MAPE (4.36–7.68% and 4.61–10.26%) and RMSE (1.21 kW–2.04 kW and 1.20 kW–2.03 kW) values, respectively. Traditional MLR and ARIMA models tend to smooth out short-term fluctuations and underperform during critical periods, particularly under transitional weather conditions in spring and autumn. CNN, DNN, and ANN models also exhibit inconsistent performance in all seasonal comparison cases, likely due to their limited capability to capture the sequential temporal dependencies inherent in surplus energy profiles. Additionally, as shown in Figure 11, the ARIMA, MLR, SVR, and RF models exhibit lower R^2 values and higher MAE values, indicating a weaker fit and less reliable forecasts. In autumn and winter, their R^2 values were (0.051, 0.504, 0.569, and 0.597) and (0.355, 0.440, 0.401, and 0.602), respectively. Meanwhile, the MAE values were highest during the spring period, reaching 1.90 kW, 2.07 kW, 1.74 kW, and 1.66 kW, and remained elevated in the summer period with values of 1.81 kW, 1.99 kW, 1.41 kW, and 1.49 kW,

respectively. This finding is attributed to several factors, most notably the nonlinear patterns and complex temporal dependencies inherent in the time-series input features.

In Figures 12 and 13, a comparison is shown between RNN-based models and the other models in terms of their performance in forecasting energy surplus availability over a 48-h-ahead horizon. The comparison reveals that RNN, BiLSTM, LSTM, and GRU models could produce more accurate forecasts, with outputs that more closely align with the actual data during certain periods. The overall enhancement in forecasting accuracy with these models is evident in the lower MAPE values, as shown in Figure 12. Notably, all four models, LSTM, BiLSTM, GRU, and RNN, maintained the lowest MAPE values during the winter period, approximately 3.98%, 4.11%, 5.07%, and 5.48%, respectively. Among them, BiLSTM consistently delivered the best overall performance in all seasonal comparison cases, highlighting its capability in capturing complex temporal dependencies over longer horizons. GRU and LSTM models also performed reliably; however, GRU showed a slight tendency to underpredict during periods of high onsite generation, as indicated by elevated RMSE values in the summer and spring datasets. The standard RNN model remains competitive but exhibits slightly less consistency than its gated counterparts.

Conversely, the traditional ARIMA, MLR, RF, and SVR models showed a noticeable degradation in performance. Their MAPE and RMSE values increased substantially, reflecting their limited capability to capture long-term temporal patterns. As illustrated in Figure 13, these models have significantly higher MAEs and lower R^2 values, indicating a poor fit and reduced forecasting accuracy as the forecasting horizon extends. Similarly, the neural network models (CNN, DNN, and ANN) failed to match the temporal resolution and adaptability achieved by recurrent architectures, particularly in seasons with high variability, such as spring and summer. Figures 12 and 13 both demonstrate the superior capability of RNN-based models to provide accurate forecasts of surplus energy profiles over the 48-h horizon. This analysis of the 24 h/24 h scenario also reveals the effectiveness of these models in forecasting surplus energy availability across all considered seasons (Appendix A). RNN-based models achieved superior accuracy in both 24 h and extended 48-h-ahead forecasts, as evidenced by their lower MAPE, RMSE, and MAE values and their higher R^2 values. The following section extends this analysis to the 24 h/48 h scenario, providing further insight into the models' capabilities under more dynamic operational conditions.

4.2.2. Surplus Forecast Models for the 24 h/48 h Scenario

This section shows a comparative analysis of surplus energy availability forecasts focusing on the second scenario, which assumes fixed surplus energy profiles available at 24-h intervals and variable energy demand aggregated over 48 h, as defined by Equation (5). This contrasts with the first scenario, which maintains a fixed generation–demand pattern at 24-h intervals, as described in Equation (4). This scenario reflects more dynamic real-world conditions, where surplus energy generated beyond a single day can be leveraged to optimize flexible energy consumption and maximize EV charging opportunities. Figures 14–17 show the performance results of various forecasting models under this scenario, using the same input features as in the previous cases. Figures 14 and 15 specifically illustrate the performance of the developed models in forecasting surplus energy availability over a 24-h-ahead horizon. As expected, the RNN, BiLSTM, LSTM, and GRU models consistently achieved lower MAPE, RMSE, and MAE values in most cases, reaffirming their strength in capturing short-term temporal dependencies. Specifically, BiLSTM achieved the best overall performance across all seasonal comparisons, with MAPE, RMSE, and MAE values not exceeding (3.53%, 1.89 kW, 1.05 kW), (4.56%, 2.16 kW, 1.33 kW), (4.03%, 1.31 kW, 0.65 kW), and (3.36%, 1.58 kW, 0.74 kW) for summer, spring, autumn, and winter, respectively. This outcome is further supported by the relatively higher R^2 values, demonstrating significant

consistency between the forecasted outputs and the actual data patterns. This superior performance is attributed to the bidirectional processing mechanism of the BiLSTM architecture, which enables the model to effectively learn and capture information from both past and future time steps. The primary advantage of BiLSTM lies in its ability to enhance contextual knowledge by processing input sequences in both forward and backward directions, then concatenating the two outputs into a unified contextual representation.

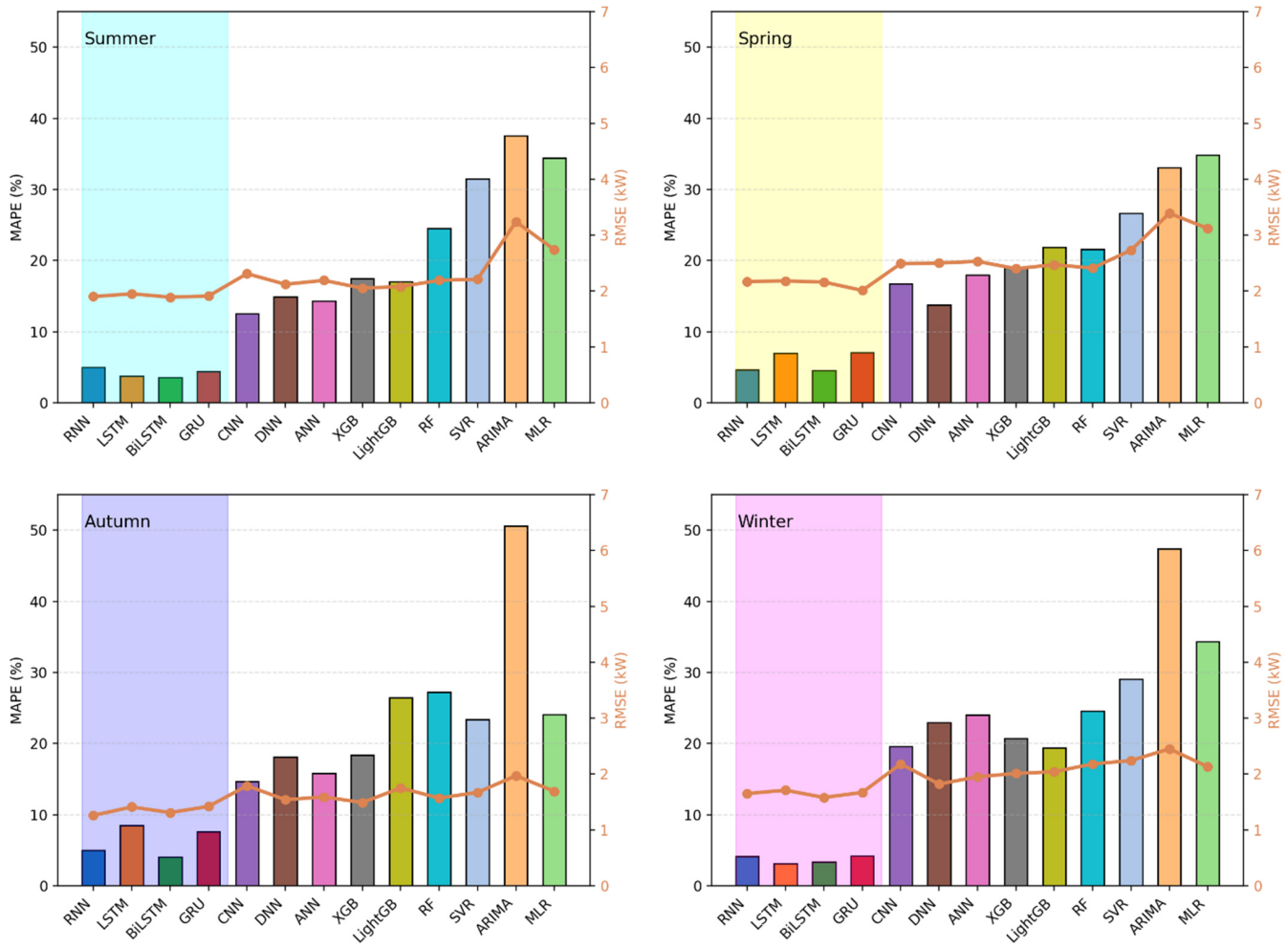


Figure 14. Comparison of MAPE and RMSE values for various RNN-based models and their counterparts of common data-driven models in forecasting energy surplus under the second scenario over a 24-h-ahead horizon.

On the other hand, traditional models such as ARIMA, MLR, SVR, and RF exhibited lower accuracy in forecasting surplus energy availability, as indicated by higher MAPE and RMSE values, as shown in Figure 14. This is further evidenced by poor alignment with the actual data patterns and quantitatively supported by unimproved MAE and R^2 values, as illustrated in Figure 15. Similarly, the XGB, LightGB, ANN, DNN, and CNN models struggled to maintain predictive accuracy, particularly during autumn and winter, when sunlight patterns are less consistent. This limitation was expected due to the nature of the datasets used in these seasons, which are distinguished by nonlinear fluctuations and irregular, sharp patterns, posing additional challenges for accurate forecasting.

Subsequent comparisons, as illustrated in Figures 16 and 17, focus on the forecasted results considering a 48-h-ahead horizon. These comparisons demonstrate that the RNN, BiLSTM, LSTM, and GRU models forecast surplus energy availability more accurately than their traditional counterparts, including models such as ANN, DNN, and CNN. In this

context, Figure 17 illustrates a comprehensive overview of the statistical performance across all seasons, highlighting MAE and R^2 values. The higher R^2 values observed indicate a strong fit and closer alignment with the actual data patterns for all seasonal comparison cases. Supporting this, a closer examination of the forecasted and actual values within the representative figures (Figures A4 and A5 in Appendix B) reveals specific instances where the RNN architecture-based models successfully captured sharp fluctuations and peak values in the actual surplus energy data. Among the evaluated models, BiLSTM consistently achieved the best performance due to its ability to learn bidirectional temporal dependencies, allowing it to better capture both past and near-future patterns in surplus energy time series. Simultaneously, model performance varied across seasons, reflecting differences in solar availability and demand patterns, with generally higher accuracy observed during summer months and increased forecasting uncertainty during spring periods. This finding indicates that carefully applying RNN-based models, combined with proper hyperparameter tuning and selection of relevant temporal features, can greatly improve the forecasting model's capacity to capture the complex dynamics of surplus energy availability in micro-residential communities, especially when tackling the challenges posed by nonlinear and seasonally irregular dataset patterns.

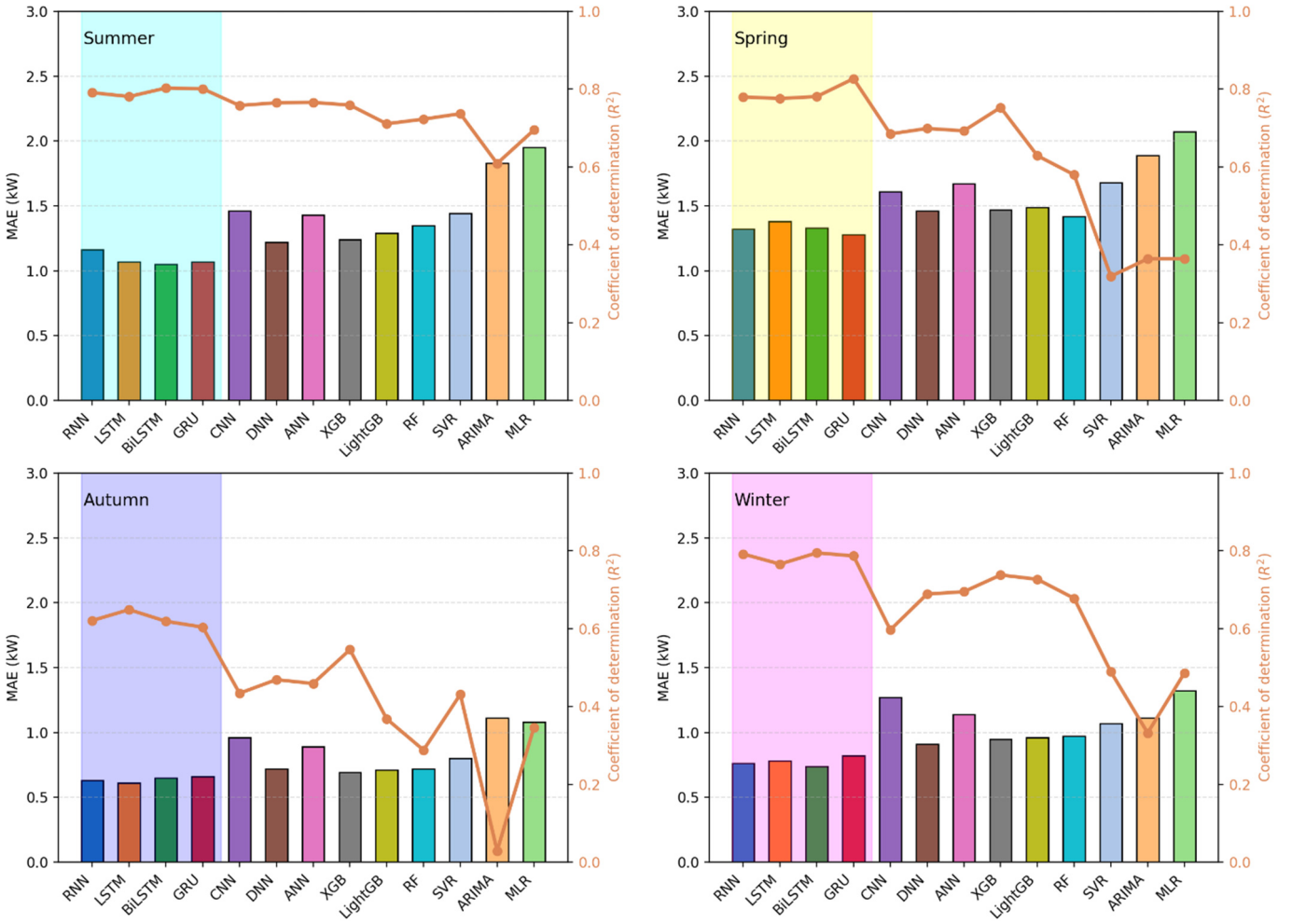


Figure 15. Comparison of MAE and R^2 values for various RNN-based models and their counterparts of common data-driven models in forecasting energy surplus under the second scenario over a 24-h-ahead horizon.

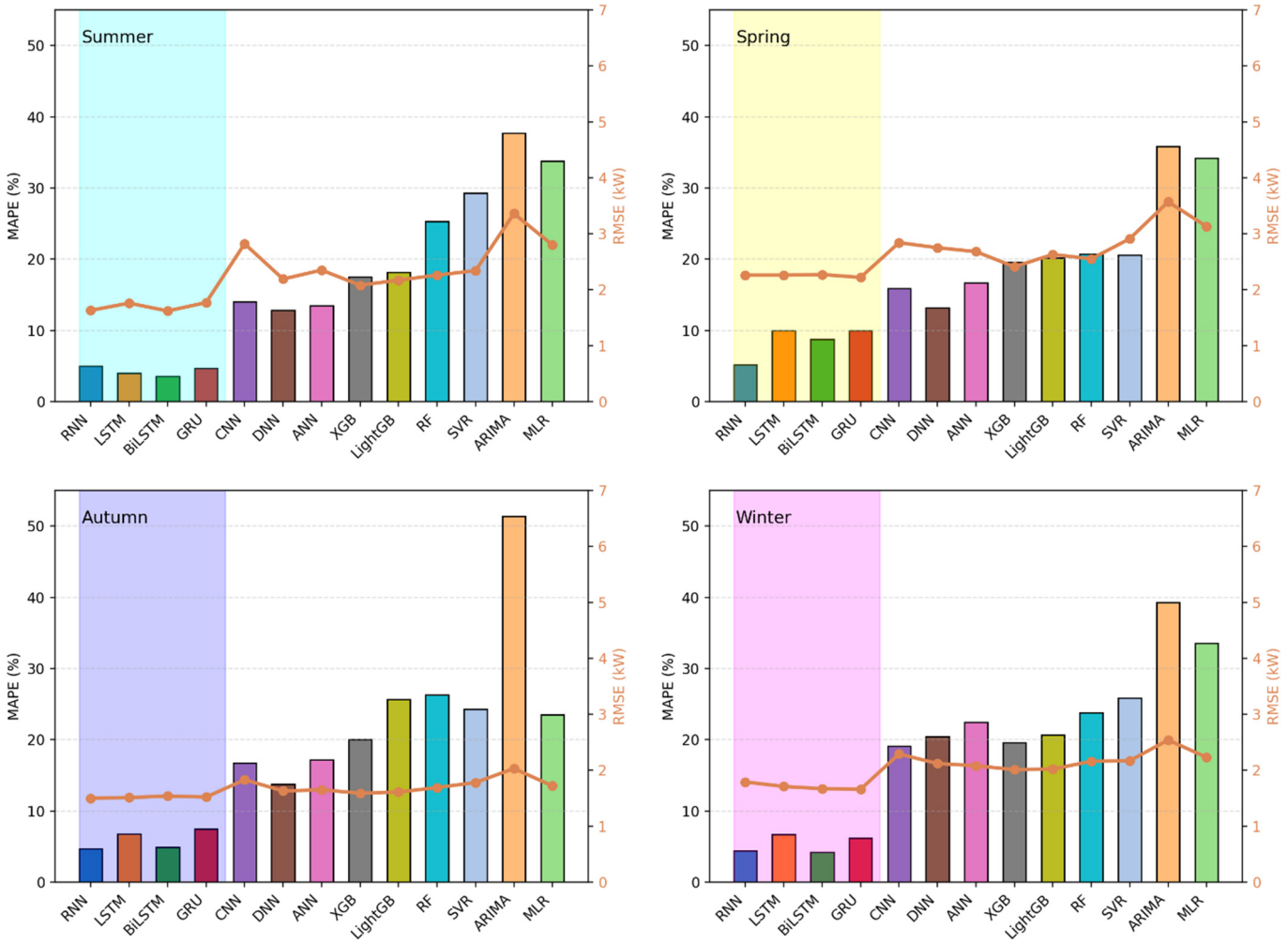


Figure 16. Comparison of MAPE and RMSE values for various RNN-based models and their counterparts of common data-driven models in forecasting energy surplus under the second scenario over a 48-h-ahead horizon.

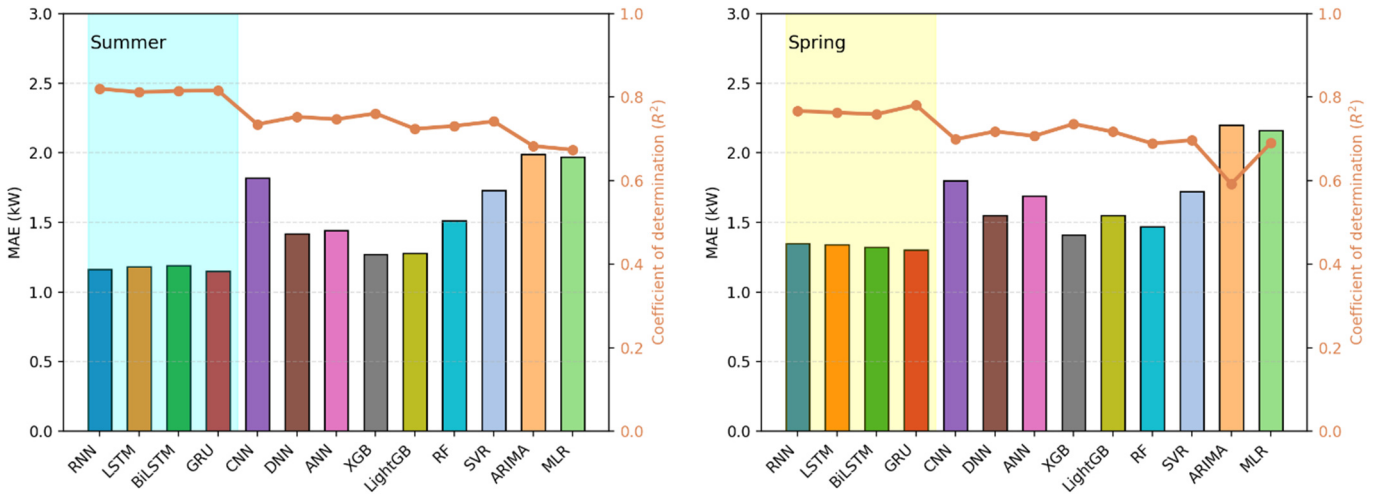


Figure 17. *Cont.*

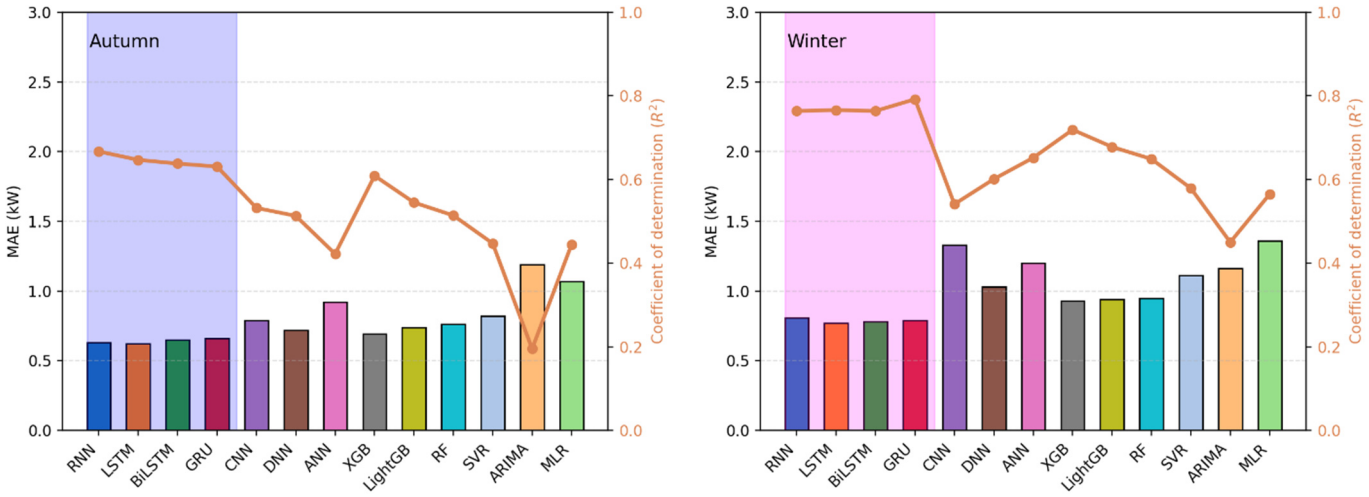


Figure 17. Comparison of MAE and R^2 values for various RNN-based models and their counterparts of common data-driven models in forecasting energy surplus under the second scenario over a 48-h-ahead horizon.

4.3. Scheduling of Surplus Availability

In the previous sections, the global performance indices (MAPE, RMSE, MAE, and R^2) for the different forecasting models were analyzed as a function of both the time horizons and the scale of surplus energy availability in the micro-residential community. In this section, to develop a deeper understanding of how the outputs of each RNN architecture-based model can be managed, the forecasted surplus energy values are visualized and discussed in terms of their ability to meet the EV charging schedules. To achieve this, the charging potential is assessed using three commonly available EV models in the study area: Renault Zoe (with a stable battery capacity of 22 kWh), Renault Twingo (with a stable battery capacity of 23 kWh), and Renault Mégane E-Tech EV40 (with a stable battery capacity of 40 kWh). The forecasted surplus energy values generated under the first scenario (24 h/24 h) with a 48-h prediction horizon for the four RNN-based models are used in this analysis. Figures 18–20 illustrate the model-based charging schedule results for all seasons, which were calculated by dividing the hourly forecasted surplus energy by the corresponding battery capacity of each EV model, thereby indicating how well the forecasted surplus energy values align with the EV charging demands (i.e., expressed by y, the number of charging status occurrences).

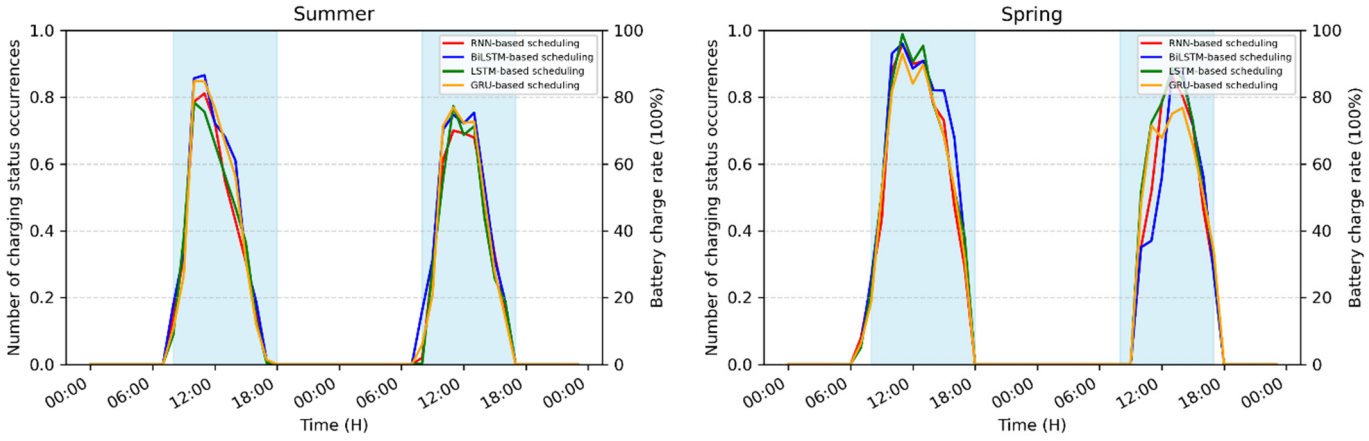


Figure 18. *Cont.*

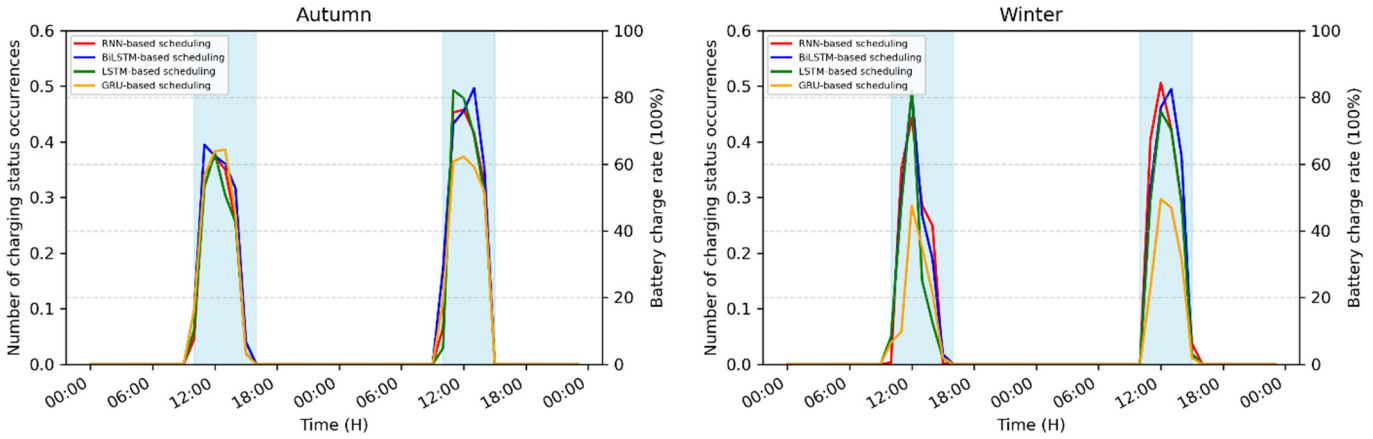


Figure 18. Renault Zoe model charging management based on an RNN-based model schedules using 48-h-ahead forecasts under the first scenario (24 h/24 h).

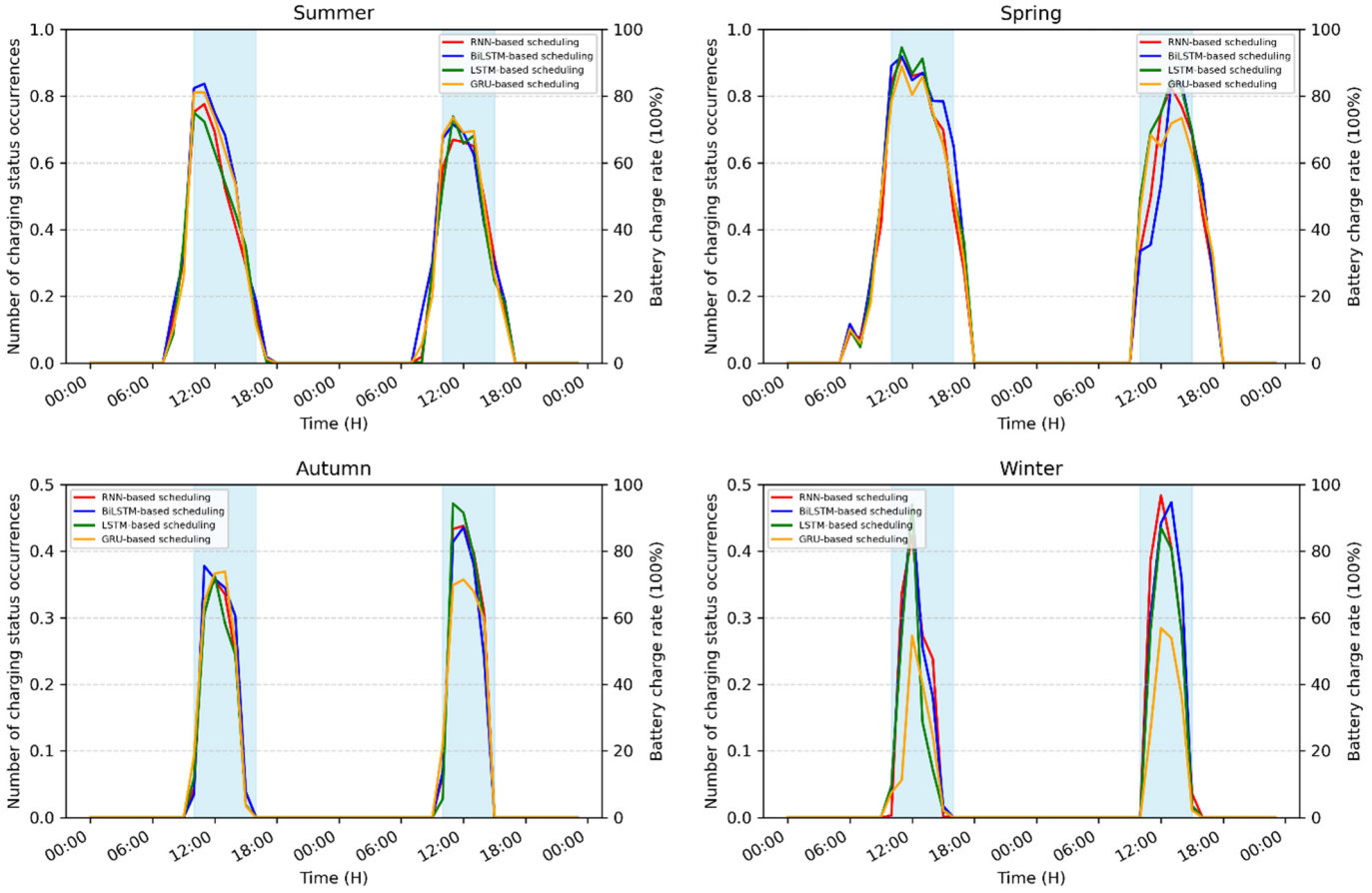


Figure 19. Renault Twingo model charging management based on an RNN-based model schedules using 48-h-ahead forecasts under the first scenario (24 h/24 h).

Figure 18 presents the charging potential of the Renault Zoe model using the 48-h-ahead surplus energy forecasts from the four RNN-based models under the first scenario (24 h/24 h). The y-axis shows the number of charging status occurrences, obtained by dividing the hourly forecasted surplus energy by the battery capacity of 22 kWh. This figure illustrates how often surplus energy is sufficient to initiate a full or partial charging cycle, enabling a direct interpretation of forecast utility in real-world EV integration. Figure 19 provides a similar analysis for the Renault Twingo model, which has a slightly larger battery capacity of 23 kWh. The results highlight how the model-specific battery size influences the charging frequency supported by forecasted surplus energy. Notably, small

changes in capacity can slightly alter the charging event profiles derived from the same forecast data, demonstrating the importance of aligning model forecasts with actual EV fleet characteristics.

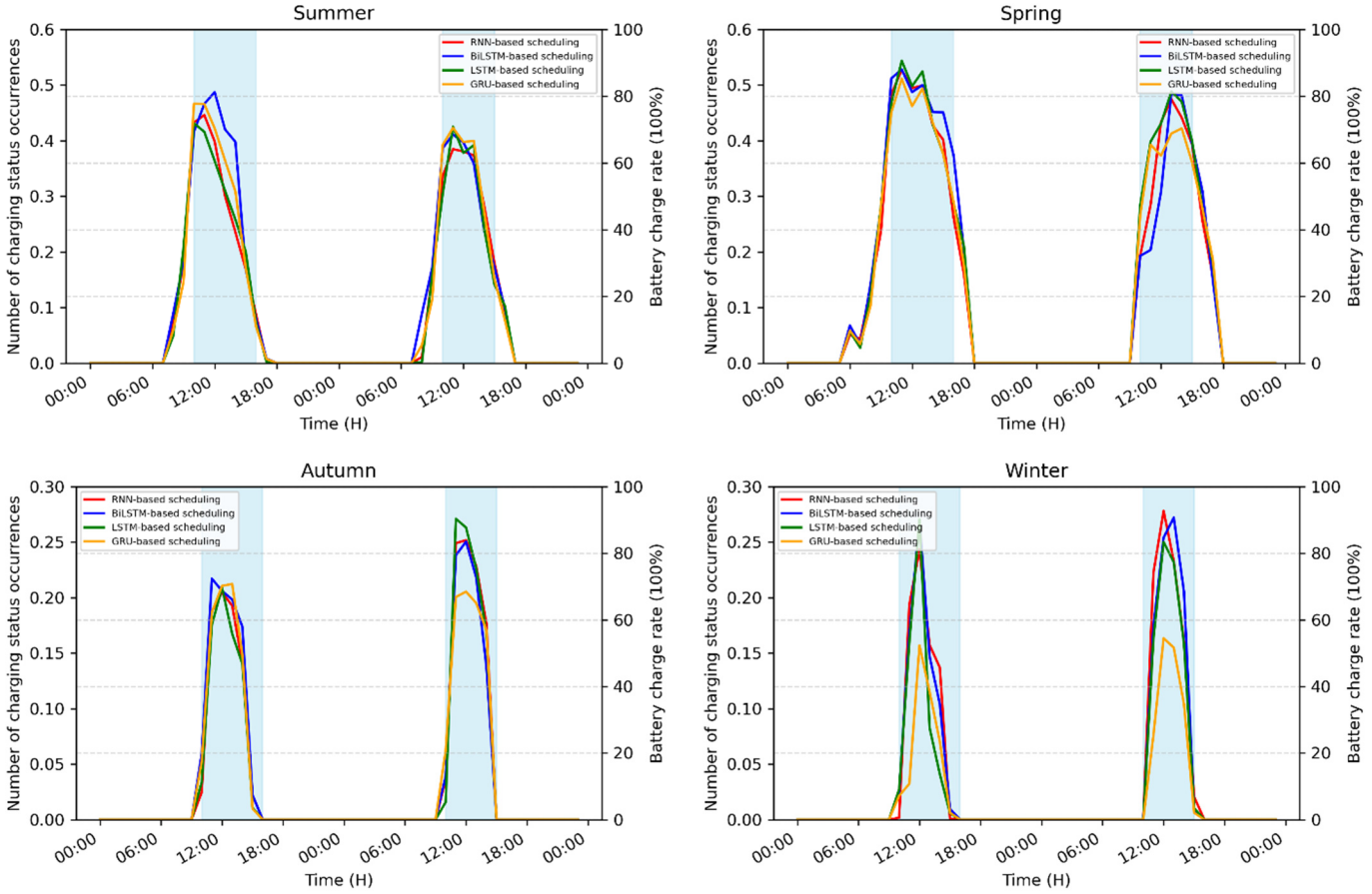


Figure 20. Renault Megane model charging management based on an RNN-based model schedules using 48-h-ahead forecasts under the first scenario (24 h/24 h).

Figure 20 depicts the charging management results for the Renault Mégane E-Tech EV40, which has the largest battery among the three at 40 kWh. The lower frequency of charging status occurrences in this case reflects the higher energy requirement per full charge. This figure further emphasizes how the forecasted surplus, though the same in absolute terms, offers different levels of utility depending on the battery capacity of the vehicle model being considered. Together, these figures provide a practical perspective on how accurate surplus energy forecasts, when combined with knowledge of battery specifications, can directly inform and optimize EV charging schedules in micro-residential, community-scale energy systems.

From an operational standpoint, small forecast deviations are expected to result mainly in minor shifts in EV charging start times or partial utilization of available surplus energy, rather than significant charging delays or failures, since charging schedules operate within flexible time windows and can be adjusted in near real time using updated surplus estimates or limited grid support. Therefore, the forecasting accuracy achieved by the RNN-based models is operationally sufficient to enable effective smart charging strategies while maintaining system reliability.

4.4. Limitations

While the proposed RNN-based forecasting framework demonstrates promising predictive performance, three main limitations of this study are acknowledged. First, the forecasting models were developed using data from only six single-family detached houses to represent a micro-residential community. This limited sample may not fully capture the variability present in larger surplus energy profiles of single-family detached house groups in larger communities, although it provides a useful proof-of-concept for short-term surplus energy forecasting. Second, the study relies on simulated rooftop PV energy generation, which may not capture the full complexity, stochasticity, and operational uncertainties of real-world PV systems. Seasonal data were used to reflect variations in solar radiation and surplus energy availability, providing a realistic basis for model training, but further validation using real-world PV measurements is needed. Third, household demand data were not included due to availability constraints. Incorporating historical demand could improve short-term surplus energy forecasting, particularly during periods of high load variability, and is an important avenue for future work. Additionally, the comparative analysis relied on performance metrics without formal statistical tests such as the paired *t*-test and the Wilcoxon signed-rank test to confirm the significance of differences between models, which could further substantiate the relative superiority of the proposed RNN-based approaches. Future work should validate the models using larger datasets, diverse building types, real-world PV generation, and historical household demand to enhance generalizability and assess architecture-specific performance under varying environmental conditions. To this end, real-world deployment would require high-resolution smart meter data, measured PV outputs, and EV charging logs, together with adaptations for real-time data acquisition, periodic model updating, and integration with operational energy and charging management systems.

5. Conclusions

This study developed a data-driven framework based on RNN architecture-based methods to address the challenges of short-term time-series forecasting for surplus energy availability in the context of micro-residential communities. Two operational scenarios were considered, using seasonally segmented hourly datasets. Prototype single-family detached house models equipped with rooftop PV systems were employed to generate sequential input and output datasets, supporting the development of RNN-based models: standard RNN, BiLSTM, LSTM, and GRU. Seasonal periods were delineated as follows: winter (22 December to 21 March), spring (22 March to 20 June), summer (21 June to 22 September), and autumn (22 September to 21 December). Pearson correlation coefficient analysis was incorporated into the data preprocessing pipeline to identify the most relevant factors by estimating the correlations between surplus energy availability and outdoor environmental variables, thereby informing input feature selection and enhancing forecasting performance.

Using the simulated datasets, advanced RNN models, namely RNN, BiLSTM, LSTM, and GRU, were developed and evaluated alongside common data-driven models (ARIMA, MLR, SVR, RF, LightGB, XGB, ANN, DNN, and CNN) under two forecasting strategies for surplus availability estimates: 24 h/24 h and 24 h/48 h. The 24 h/24 h scenario assumes fixed onsite generation and demand over each 24-h period, whereas the 24 h/48 h scenario assumes fixed onsite generation with variable demand aggregated over 48 h. These scenarios were applied to seasonally segmented datasets to address the inherent variability and fluctuations in short-term surplus energy generation, particularly for short-term forecasting horizons not exceeding 48 h. The study yielded several key conclusions, most notably the following:

1. Model performance: All RNN architecture-based models effectively captured the temporal dependencies and seasonal variations in surplus energy availability patterns over short-term forecasting horizons, not exceeding 48 h. Among these models, the BiLSTM consistently achieved the highest accuracy, as indicated by the lowest MAPE, RMSE, and MAE values, and the highest R^2 values in correlation with actual surplus values across most seasonal comparison cases. Notably, the model achieved MAPE values of 3.53%, 4.11%, 4.56%, and 8.83%; RMSE values of 1.62 kW, 1.22 kW, 2.03 kW, and 1.20 kW; MAE values of 1.05 kW, 0.82 kW, 1.33 kW, and 0.53 kW; and R^2 values of 0.836, 0.795, 0.781, and 0.725 for the summer, winter, spring, and autumn surplus energy forecasts, respectively.
2. Impact seasonal and nonlinear patterns: This study highlighted the influence of nonlinear fluctuations and seasonally irregular data patterns on model performance. Despite these challenges, the RNN architecture-based models demonstrated notable improvements in providing accurate estimates of short-term surplus energy availability at the micro-residential community level. This was reflected in their closer alignment with actual surplus data and their stronger performance across both the 24 h/24 h and 24 h/48 h estimation scenarios.
3. Forecasting challenges: Accurate short-term forecasts remain challenging, particularly during midday peaks and seasonal transitions. These results underscore the need for more refined models and additional research that more accurately reflect real-world environmental conditions in micro-residential communities, particularly with regard to the orientation of distributed PV modules and their corresponding surplus energy generation. This would enhance the accuracy of short-term forecasts during transitional daylight periods, which is crucial for supporting EV charging schedules more effectively and reliably and advancing the broader transition toward sustainable community energy systems.

Based on the above, future research ought to explore the applicability of these models in more practical scenarios by integrating them with hybrid deep learning architectures, such as transformer-RNNs and temporal attention mechanisms, to address a broader range of micro-residential communities and surplus energy availability patterns under realistic environmental scenarios, while accounting for nonlinear behaviors and irregular fluctuations. Moreover, advancing data-driven methods for forecasting residential energy demand and onsite energy generation dynamics using actual datasets is essential to enhance both the performance and adaptability of the model. This progression supports the development of sophisticated black-box methods capable of enabling real-time EV charging scheduling as a scalable solution within residential communities.

Author Contributions: All authors of this paper have made objective contributions within the scope of their respective job responsibilities, as detailed below: A.A.A.G.; Conceptualization, methodology, software, validation, formal analysis, visualization, investigation, resources, writing—original draft preparation, writing—review and editing, M.N.; data curation, and E.F.; supervision. All authors have read and agreed to the published version of the manuscript.

Funding: This research received no external funding.

Data Availability Statement: The datasets and analyses used in this paper will be made available on reasonable request.

Conflicts of Interest: The authors declare no conflicts of interest.

Appendix A

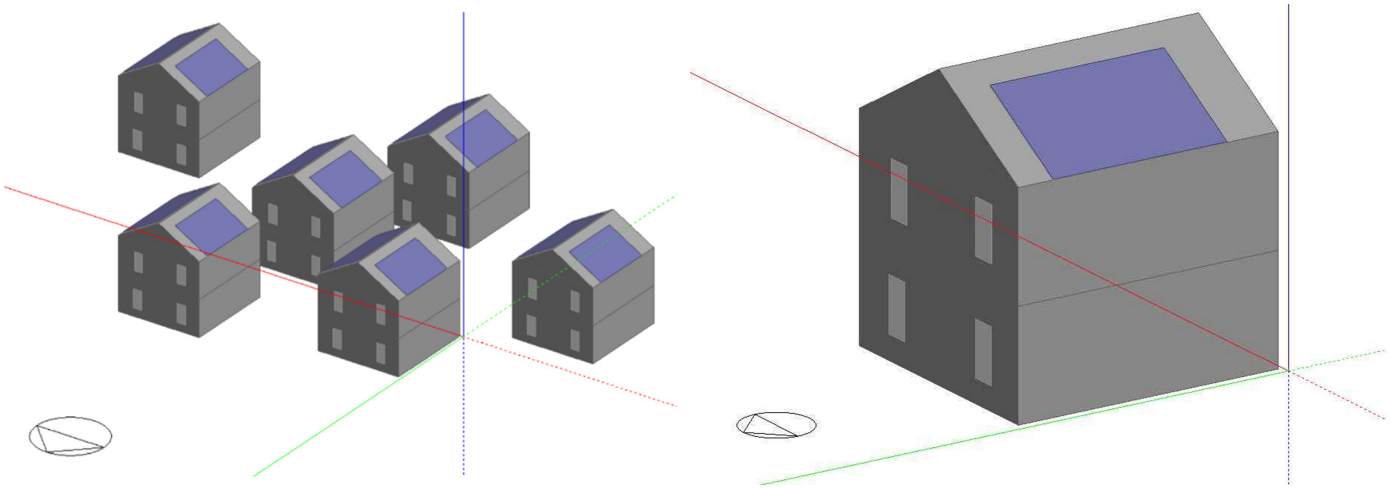


Figure A1. Initial prototype models of a single-family detached house used to simulate each building over a typical year using climate data.

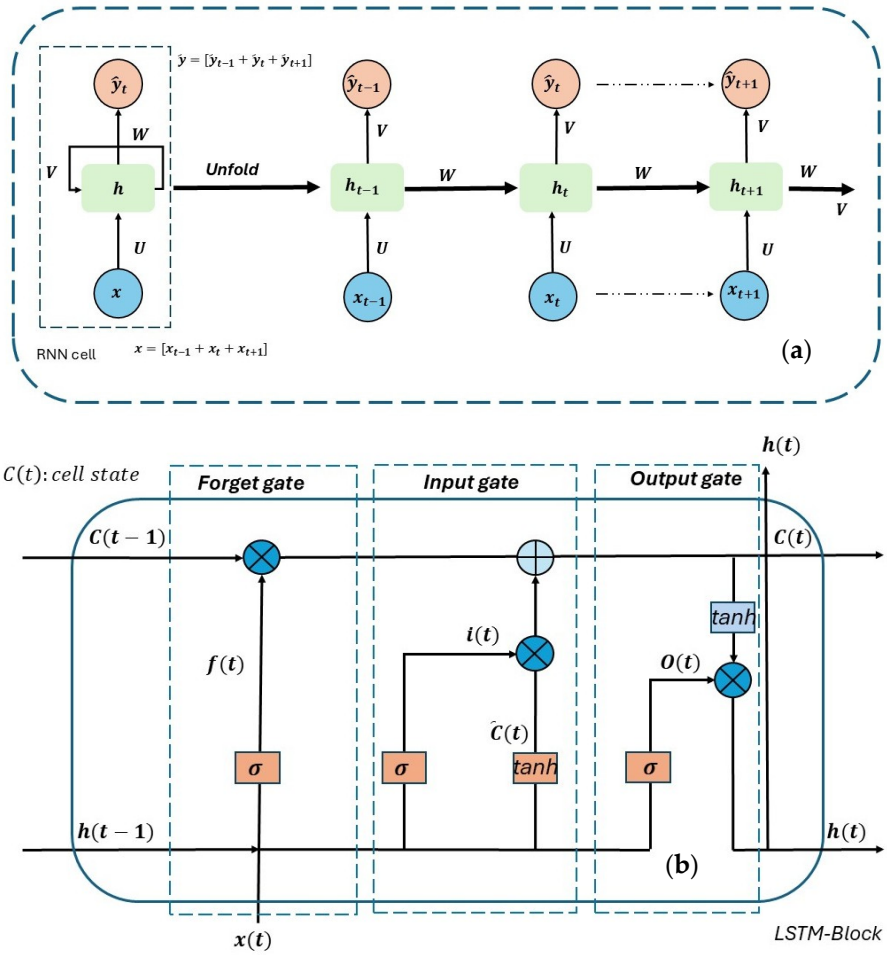


Figure A2. Basic network structures for (**a**) a single RNN unit and (**b**) a single LTSM unit.

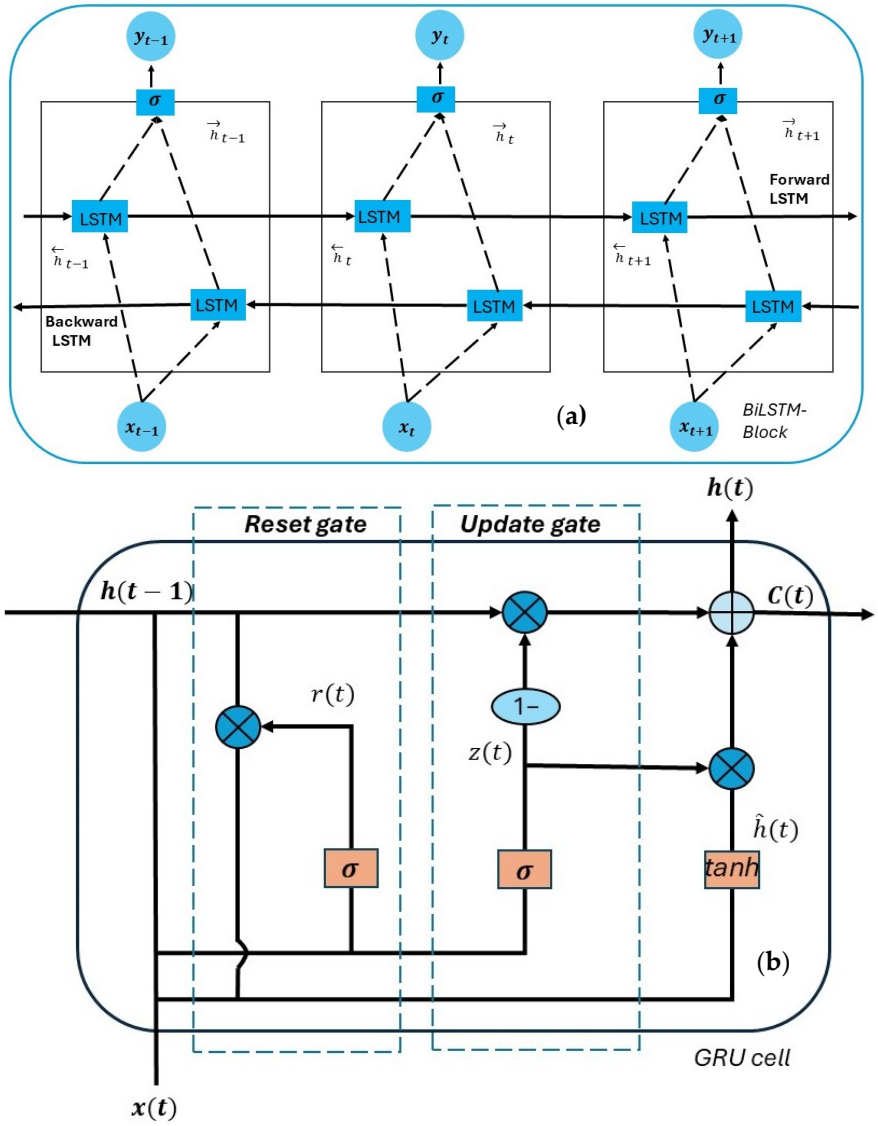


Figure A3. Neural network structures for (**a**) a single BiLSTM unit and (**b**) a single GRU.

Table A1. Performance of RNN models compared to common data-driven models in forecasting surplus energy availability under the first scenario (24 h-to-24 h).

Period	Model	24-h Ahead Forecasts				48-h Ahead Forecasts			
		R^2	MAE	RMSE	MAPE	R^2	MAE	RMSE	MAPE
Summer	RNN	0.790	1.12	1.32	7.68	0.844	1.24	2.28	10.79
	LSTM	0.763	1.11	1.97	14.22	0.838	1.20	2.26	17.51
	BiLSTM	0.789	1.18	2.01	10.26	0.836	1.19	2.27	13.11
	GRU	0.750	1.08	1.95	16.71	0.837	1.19	2.22	19.48
	CNN	0.747	1.56	2.39	25.91	0.761	1.64	2.57	29.96
	DNN	0.738	1.30	5.93	29.49	0.827	1.33	5.47	23.13
	ANN	0.661	1.39	6.05	38.32	0.818	1.48	2.33	39.43
	XGB	0.746	1.41	2.91	21.86	0.798	1.30	2.54	22.28
	LightGB	0.702	1.39	2.98	19.71	0.789	1.39	2.62	20.66
	RF	0.742	1.49	3.08	24.56	0.822	1.45	2.85	25.02
	SVR	0.731	1.41	2.36	29.06	0.784	1.46	2.48	29.34
	MLR	0.715	1.99	2.75	48.70	0.766	2.02	2.78	35.99
	ARIMA	0.624	1.81	3.19	42.25	0.668	1.98	3.32	48.47

Table A1. *Cont.*

Period	Model	24-h Ahead Forecasts				48-h Ahead Forecasts			
		R^2	MAE	RMSE	MAPE	R^2	MAE	RMSE	MAPE
Spring	RNN	0.663	1.45	2.04	5.16	0.743	1.23	2.11	4.15
	LSTM	0.646	1.48	2.06	8.06	0.743	1.37	2.15	8.52
	BiLSTM	0.694	1.38	2.03	6.18	0.751	1.14	2.03	7.01
	GRU	0.663	1.46	2.01	7.95	0.743	1.36	2.10	9.92
	CNN	0.598	1.72	2.69	18.82	0.725	1.78	2.89	22.02
	DNN	0.544	1.60	2.61	15.58	0.708	1.57	2.60	16.82
	ANN	0.523	1.70	2.58	19.63	0.729	1.72	2.71	17.32
	XGB	0.602	1.59	2.49	22.19	0.721	1.44	2.57	21.17
	LightGB	0.599	1.61	2.65	22.63	0.719	1.52	2.60	21.63
	RF	0.583	1.66	2.79	23.33	0.718	1.51	2.61	22.74
	SVR	0.525	1.74	2.74	24.91	0.707	1.72	2.93	23.02
	MLR	0.481	2.07	3.02	33.04	0.697	2.11	3.10	33.02
	ARIMA	0.433	1.90	3.39	35.03	0.605	1.98	3.54	37.09
Autumn	RNN	0.713	0.54	1.21	6.72	0.693	0.62	1.20	7.49
	LSTM	0.653	0.58	1.25	10.44	0.651	0.64	1.30	13.65
	BiLSTM	0.725	0.53	1.20	6.48	0.680	0.69	1.14	8.83
	GRU	0.663	0.54	1.22	9.67	0.663	0.73	1.27	9.56
	CNN	0.562	0.77	1.62	21.59	0.510	0.99	1.59	20.97
	DNN	0.604	0.64	1.61	18.72	0.611	0.94	1.88	18.26
	ANN	0.594	0.72	1.59	20.51	0.619	0.89	1.56	17.75
	XGB	0.605	0.61	1.33	21.15	0.589	0.76	1.38	18.28
	LightGB	0.539	0.64	1.35	23.64	0.547	0.86	1.45	19.66
	RF	0.597	0.70	1.37	23.09	0.552	0.97	1.46	26.02
	SVR	0.569	0.80	1.59	22.66	0.508	0.91	1.69	21.34
	MLR	0.504	1.04	1.65	37.69	0.474	1.07	1.77	33.43
	ARIMA	0.051	1.28	2.03	39.25	0.137	1.48	2.11	35.99
Winter	RNN	0.667	0.71	1.21	4.36	0.724	0.804	1.80	5.48
	LSTM	0.669	0.77	1.46	3.02	0.697	0.809	1.81	3.98
	BiLSTM	0.678	0.82	1.22	4.61	0.702	0.815	1.79	4.11
	GRU	0.649	0.84	1.29	4.38	0.703	0.846	1.82	5.07
	CNN	0.488	1.17	2.08	17.37	0.559	1.01	1.97	17.30
	DNN	0.536	0.94	1.76	18.36	0.492	1.00	1.98	19.80
	ANN	0.532	1.21	2.07	19.95	0.503	1.02	2.11	21.91
	XGB	0.625	0.91	1.59	23.53	0.659	1.07	1.89	22.16
	LightGB	0.619	0.92	1.63	25.74	0.646	1.08	1.96	24.45
	RF	0.602	0.98	1.67	34.08	0.611	1.09	1.99	29.95
	SVR	0.401	1.11	2.11	28.96	0.475	1.14	2.01	28.64
	MLR	0.440	1.31	2.15	38.46	0.521	1.35	2.24	34.82
	ARIMA	0.355	1.47	2.39	48.88	0.397	1.13	2.49	39.33

Table A2. Performance of RNN models compared to common data-driven models in forecasting surplus energy availability under the second scenario (24-h to 48 h).

Period	Model	24-h Ahead Forecasts				48-h Ahead Forecasts			
		R^2	MAE	RMSE	MAPE	R^2	MAE	RMSE	MAPE
Summer	RNN	0.791	1.16	1.90	5.01	0.820	1.16	1.63	4.98
	LSTM	0.781	1.07	1.95	3.78	0.812	1.18	1.76	4.02
	BiLSTM	0.803	1.05	1.89	3.53	0.815	1.19	1.62	3.59
	GRU	0.801	1.07	1.91	4.44	0.816	1.15	1.77	4.67
	CNN	0.758	1.46	2.31	12.54	0.735	1.82	2.82	14.02
	DNN	0.765	1.22	2.12	14.92	0.753	1.42	2.19	12.81
	ANN	0.766	1.43	2.19	14.31	0.747	1.44	2.35	13.47
	XGB	0.759	1.24	2.05	17.42	0.761	1.27	2.08	17.53
	LightGB	0.711	1.29	2.08	17.03	0.724	1.28	2.17	18.19
	RF	0.723	1.35	2.19	24.48	0.731	1.51	2.26	25.28
	SVR	0.737	1.44	2.21	31.47	0.742	1.73	2.34	29.26
	MLR	0.695	1.95	2.74	34.43	0.674	1.97	2.80	33.74
	ARIMA	0.609	1.83	3.24	37.55	0.683	1.99	3.36	37.69
Spring	RNN	0.780	1.32	2.17	4.63	0.767	1.35	2.26	5.21
	LSTM	0.776	1.38	2.18	6.96	0.763	1.34	2.26	9.98
	BiLSTM	0.781	1.33	2.16	4.56	0.759	1.32	2.27	8.79
	GRU	0.827	1.28	2.01	7.03	0.781	1.30	2.22	9.94
	CNN	0.685	1.61	2.49	16.77	0.699	1.80	2.84	15.92
	DNN	0.699	1.46	2.50	13.73	0.718	1.55	2.75	13.19
	ANN	0.693	1.67	2.53	17.97	0.707	1.69	2.68	16.70
	XGB	0.753	1.47	2.40	18.96	0.736	1.41	2.41	19.58
	LightGB	0.629	1.49	2.47	21.86	0.717	1.55	2.63	20.17
	RF	0.580	1.42	2.41	21.56	0.689	1.47	2.55	20.73
	SVR	0.319	1.68	2.73	26.66	0.697	1.72	2.91	20.59
	MLR	0.299	2.07	3.12	34.82	0.690	2.16	3.13	34.18
	ARIMA	0.364	1.89	3.39	33.09	0.592	2.20	3.57	35.84
Autumn	RNN	0.621	0.63	1.26	4.99	0.667	0.63	1.50	4.71
	LSTM	0.649	0.61	1.41	8.47	0.647	0.62	1.51	6.75
	BiLSTM	0.619	0.65	1.31	4.03	0.638	0.65	1.54	4.93
	GRU	0.604	0.66	1.42	7.64	0.631	0.66	1.52	7.51
	CNN	0.434	0.96	1.79	14.68	0.532	0.79	1.83	16.77
	DNN	0.469	0.72	1.54	18.09	0.513	0.72	1.63	13.73
	ANN	0.459	0.89	1.59	15.81	0.422	0.92	1.65	17.19
	XGB	0.546	0.69	1.49	18.37	0.609	0.69	1.59	19.99
	LightGB	0.368	0.71	1.75	26.45	0.545	0.74	1.61	25.66
	RF	0.288	0.72	1.57	27.23	0.514	0.76	1.69	26.29
	SVR	0.431	0.80	1.67	23.36	0.447	0.82	1.78	24.29
	MLR	0.346	1.08	1.69	24.09	0.444	1.07	1.72	23.48
	ARIMA	0.029	1.11	1.97	50.61	0.195	1.19	2.03	51.34

Table A2. *Cont.*

Period	Model	24-h Ahead Forecasts				48-h Ahead Forecasts			
		R^2	MAE	RMSE	MAPE	R^2	MAE	RMSE	MAPE
Winter	RNN	0.792	0.76	1.65	4.11	0.764	0.81	1.76	4.43
	LSTM	0.766	0.78	1.71	3.16	0.766	0.77	1.71	6.73
	BiLSTM	0.795	0.74	1.58	3.36	0.764	0.78	1.67	4.23
	GRU	0.787	0.82	1.67	4.18	0.792	0.79	1.66	6.22
	CNN	0.597	1.27	2.18	19.57	0.541	1.33	2.29	19.08
	DNN	0.689	0.91	1.82	22.96	0.601	1.03	2.12	20.45
	ANN	0.695	1.14	1.95	24.01	0.652	1.20	2.08	22.41
	XGB	0.738	0.95	2.01	20.79	0.719	0.93	2.01	19.60
	LightGB	0.727	0.96	2.04	19.40	0.678	0.94	2.02	20.66
	RF	0.678	0.97	2.18	24.56	0.649	0.95	2.16	23.82
	SVR	0.489	1.07	2.24	29.06	0.579	1.11	2.17	25.85
	MLR	0.486	1.32	2.13	34.33	0.565	1.36	2.23	33.56
	ARIMA	0.332	1.11	2.45	47.40	0.450	1.16	2.54	39.29

Appendix B

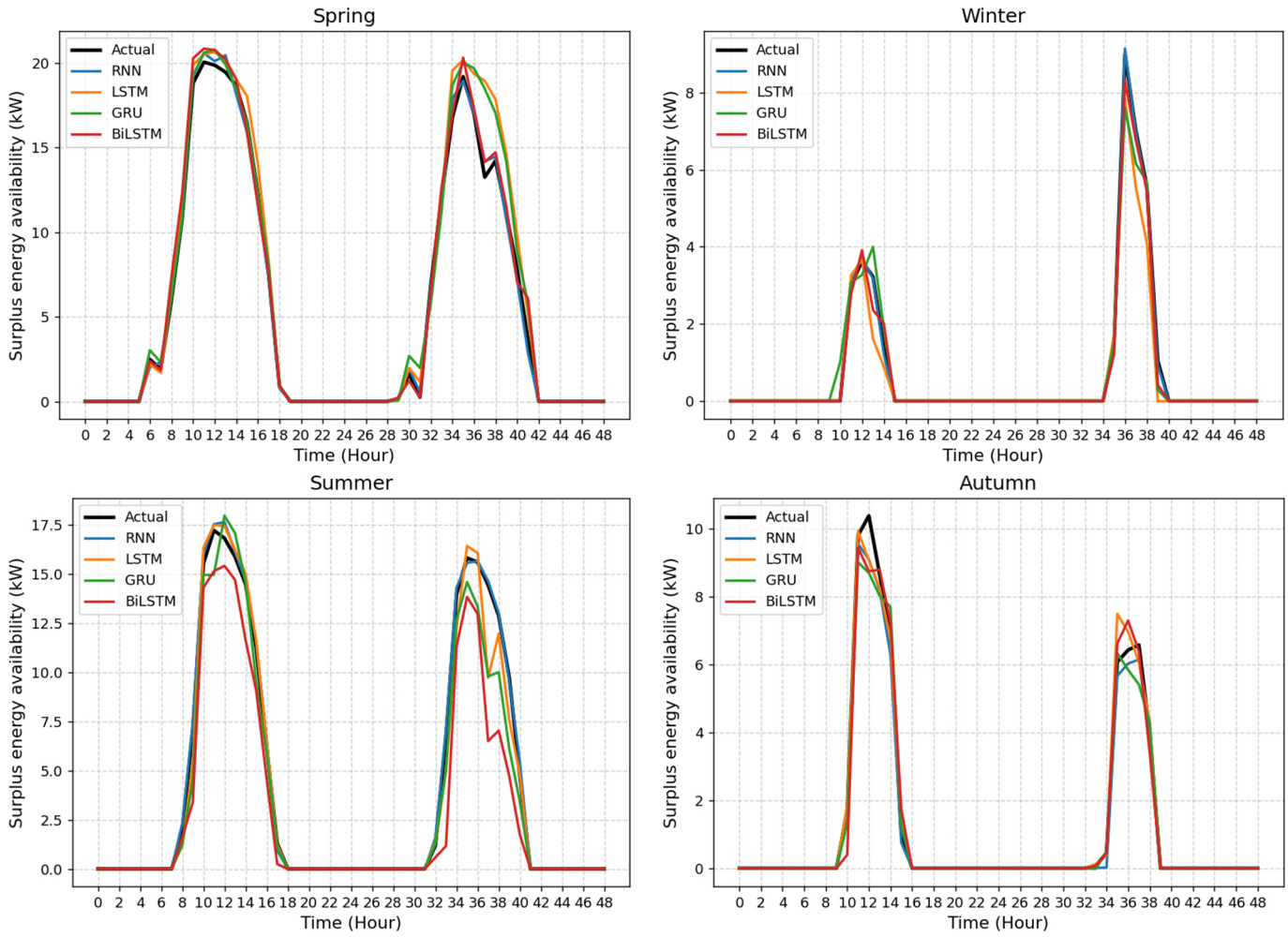


Figure A4. Comparison of surplus energy forecasts with RNN-based models considering the second scenario (24 h-to-48 h) over a 48-h horizon.

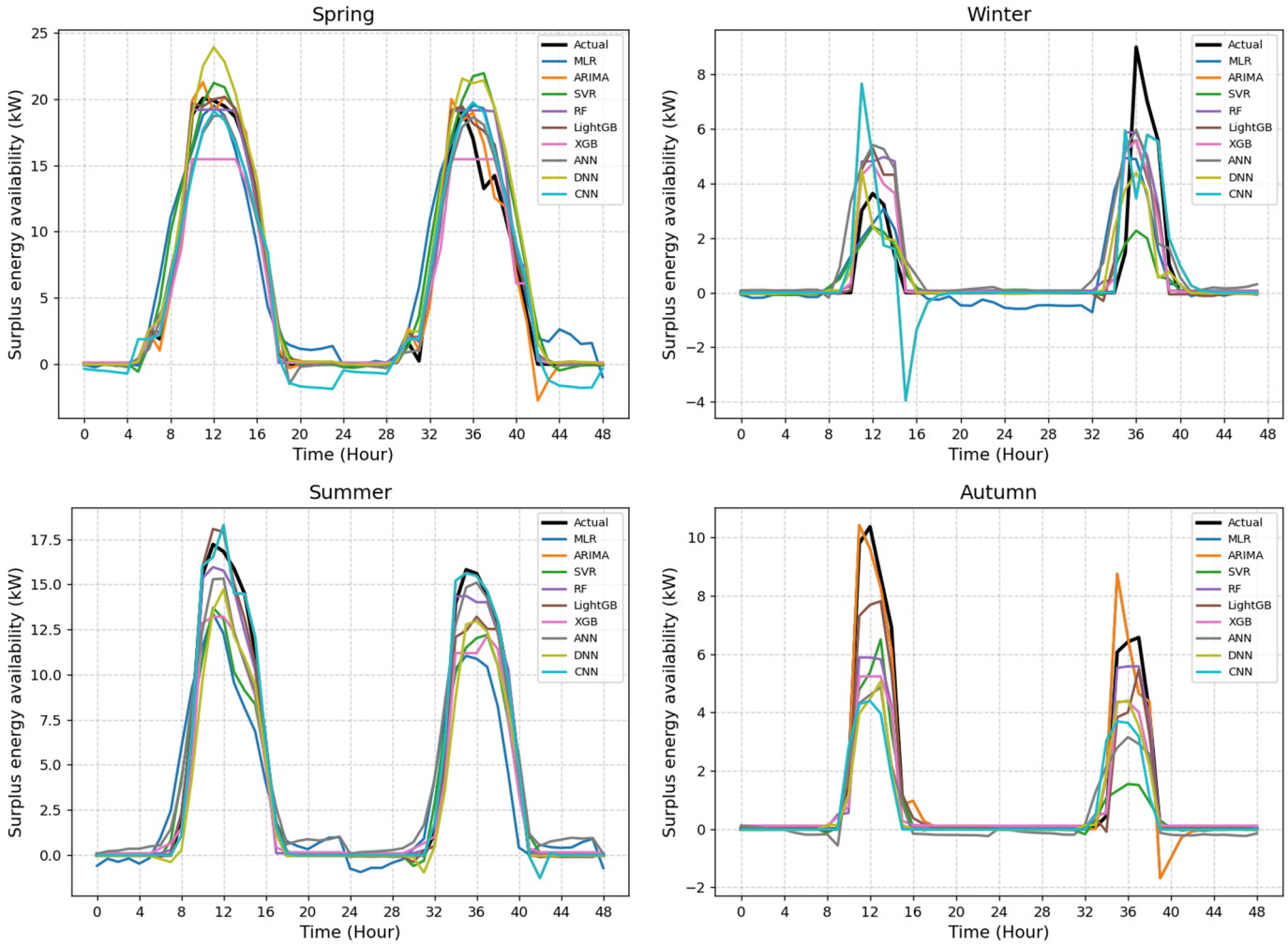


Figure A5. Comparison of surplus energy forecasts with common data-driven models considering the second scenario (24 h-to-48 h) over a 48-h horizon.

References

1. Hanif Ramadhani, U.; Fachrizal, R.; Shepero, M.; Munkhammar, J.; Widen, J. Probabilistic load flow analysis of electric vehicle smart charging in unbalanced LV distribution systems with residential photovoltaic generation. *Sustain. Cities Soc.* **2021**, *72*, 103043. [CrossRef]
2. Zhang, S.; Thoelen, K.; Peirelinck, T.; Deconinck, G. Accelerating a consensus-based EV smart charging algorithm by user priority clustering. *Sustain. Cities Soc.* **2024**, *106*, 105392. [CrossRef]
3. IEA. Technology and Innovation Pathways for Zero-Carbon-Ready Buildings by 2030: A strategic Vision from the IEA Technology Collaboration Programmes. Reports, September 2022. Available online: https://www.iea.org/reports/technology-and-innovation-pathways-for-zero-carbon-ready-buildings-by-2030 (accessed on 1 July 2025).
4. Fachrizal, R.; Munkhammar, J. Improved photovoltaic self-consumption in residential buildings with distributed and centralized smart charging of electric vehicles. *Buildings* **2020**, *13*, 1153. [CrossRef]
5. Khalid, M.; Thakur, J.; Bhagavathy, S.M.; Topel, M. Impact of public and residential smart EV chagrining on distribution power grid equipped with storage. *Sustain. Cities Soc.* **2024**, *104*, 105272. [CrossRef]
6. Fachrizal, R.; Shepero, M.; van der Meer, D.; Munkhammar, J. Smart charging of electric vehicles considering photovoltaic power production and electricity: A review. *eTransportation* **2020**, *4*, 100056. [CrossRef]
7. Dik, A.; Kutlu, C.; Sun, H.; Calautit, J.K.; Boukhanouf, R.; Omer, S. Towards sustainable urban living: A holistic energy strategy for electric vehicle and heat pump adoption in residential communities. *Sustain. Cities Soc.* **2024**, *107*, 105412. [CrossRef]
8. Pastore, L.M. Combining power-to-heat and power-to-vehicle strategies to provide system flexibility in smart urban energy districts. *Sustain. Cities Soc.* **2023**, *94*, 104548. [CrossRef]
9. Shabbir, N.; Kutt, L.; Astapov, V.; Daniel, K.; Jawad, M.; Husev, O.; Rosin, A.; Martins, J. Enhancing PV hosting capacity and mitigating congestion in distribution networks with deep learning based PV forecasting and battery management. *Appl. Energy* **2024**, *372*, 123770. [CrossRef]

10. Luthander, R.; Widen, J.; Nilsson, D.; Palm, J. Photovoltaic self-consumption in buildings: A review. *Appl. Energy* **2015**, *142*, 80–94. [CrossRef]
11. Liao, W.; Xiao, F.; Li, Y.; Zhang, H.; Peng, J. A comparative study of demand-side energy management strategies for building integrated photovoltaics-battery and electric vehicles (EVs) in diversified building communities. *Appl. Energy* **2024**, *361*, 122881. [CrossRef]
12. Ghanavati, F.; Matias, J.C.O.; Osorio, G.J. Towards sustainable smart cities: Integration of home energy management system for efficient energy utilization. *Sustain. Cities Soc.* **2024**, *111*, 105579. [CrossRef]
13. Kazmi, H.; Munné-Collado, Í.; Mehmood, F.; Syed, T.A.; Driesen, J. Towards data-driven energy communities: A review of open-source datasets, models and tools. *Renew. Sustain. Energy Rev.* **2021**, *148*, 111290. [CrossRef]
14. Gassar, A.A.A.; Cha, S.-H. Energy prediction techniques for large-scale buildings towards a sustainable built environment: A review. *Energy Build.* **2020**, *224*, 110238. [CrossRef]
15. Bourdeau, M.; Zhai, X.-G.; Nefzaoui, E.; Guo, X.; Chatellier, P. Modeling and forecasting building energy consumption: A review of data-driven techniques. *Sustain. Cities Soc.* **2019**, *48*, 105533. [CrossRef]
16. Al-Ja'afreh, M.A.A.; Mokryani, G.; Amjad, B. An enhanced CNN-LSTM based multi-stage framework for PV and load short-term forecasting: DSO scenarios. *Energy Rep.* **2023**, *10*, 1387–1408. [CrossRef]
17. Elomari, Y.; Mateu, C.; Marin-Genesca, M.; Boar, D. A data-driven framework for designing a renewable energy community based on the integration of machine learning models with life cycle assessment and life cycle cost parameters. *Appl. Energy* **2024**, *358*, 122619. [CrossRef]
18. Lu, C.; Li, S.; Lu, Z. Building energy prediction using artificial neural networks: A literature survey. *Energy Build.* **2022**, *262*, 111718. [CrossRef]
19. Gupta, M.; Arya, A.; Varshney, U.; Mittal, J.; Tomar, A. A review of PV power forecasting using machine learning techniques. *Prog. Eng. Sci.* **2025**, *2*, 100058. [CrossRef]
20. Hasan, M.; Mifta, Z.; Papiya, S.J.; Roy, P.; Dey, P.; Salsabil, N.A.; Chowdhury, N.-U.-R.; Farrok, O. A state-of-the-art comparative review of load forecasting methods: Characteristics, perspectives, and applications. *Energy Convers. Manag. X* **2025**, *26*, 100922. [CrossRef]
21. Gassar, A.A.A. Short-term energy forecasting to improve the estimation of demand response baselines in residential neighborhoods: Deep learning vs. machine learning. *Buildings* **2024**, *14*, 2242. [CrossRef]
22. Raza, A.; Jingzhao, L.; Adnan, M.; Ahmad, I. Optimal load forecasting and scheduling strategies for smart homes peer-to-peer energy networks: A comprehensive survey with critical simulation analysis. *Results Eng.* **2024**, *22*, 102188. [CrossRef]
23. Carneiro, T.C.; Marques de Carvalho, P.C.; Alves dos Santos, H.; Batista Lima, M.A.F.; Souza Braga, A.P. Review on Photovoltaic Power and Solar Resource Forecasting: Current Status and Trends. *J. Sol. Energy Eng.* **2022**, *144*, 010801. [CrossRef]
24. Aslam, S.; Herodotou, H.; Mohsin, S.M.; Javaid, N.; Ashraf, N.; Aslam, S. A survey on deep learning methods for power load and renewable energy forecasting in smart microgrids. *Renew. Sustain. Energy Rev.* **2021**, *144*, 110992. [CrossRef]
25. Ahmad, T.; Zhang, H.; Yan, B. A review on renewable energy and electricity requirement forecasting models for smart grid and buildings. *Sustain. Cities Soc.* **2020**, *55*, 102052. [CrossRef]
26. Elbeh, M.B.; Sleiti, A.K. Analysis and optimization of concentrated solar power plant for application in arid climate. *Energy Sci. Eng.* **2021**, *9*, 784–797. [CrossRef]
27. Vaziri Rad, M.A.; Kasaeian, A.; Niu, X.; Zhang, K.; Mahian, O. Excess electricity problem in off-grid hybrid renewable energy systems: A comprehensive review from challenges to prevalent solutions. *Renew. Energy* **2023**, *212*, 538–560. [CrossRef]
28. Falaki, F.; Merabtine, A.; Denis, M. A spatio-temporal analysis of electric appliance end-use demand in the residential sector: Case study of Tours (France). *Sustain. Cities Soc.* **2021**, *65*, 102635. [CrossRef]
29. Gassar, A.A.A.; Le Dreau, J. Deep learning-based short-term energy forecasts for baselines and flexibility in residential buildings. In Proceedings of the Building Simulation 2023: 18th Conference of IBPSA, Shanghai, China, 4–6 September 2023; pp. 3001–3010. [CrossRef]
30. Eren, Y.; Küçükdemiral, I. A comprehensive review on deep learning approaches for short-term load forecasting. *Renew. Sustain. Energy Rev.* **2024**, *189*, 114031. [CrossRef]
31. Wu, Y.; Wu, Y.; Cimen, H.; Vasquez, J.C.; Guerrero, J.M. Towards collective energy community: Potential roles of microgrids and blockchain to go beyond P2P energy trading. *Appl. Energy* **2022**, *314*, 119003. [CrossRef]
32. Kim, H.; Choi, H.; Kang, H.; An, J.; Yeom, S.; Hong, T. A systematic review of the smart energy conservation system: From smart homes to sustainable smart cities. *Renew. Sustain. Energy Rev.* **2021**, *140*, 110755. [CrossRef]
33. Yu, H.; Niu, S.; Shao, Z.; Jia, Y.; Jian, L. Electric vehicles integration and vehicle-to-grid operation in active distribution grids: A comprehensive review on power architectures, grid connection standards and typical applications. *Renew. Sustain. Energy Rev.* **2022**, *168*, 112812. [CrossRef]

34. Al-Oagili, A.S.; Juhana, T.; Rahmat, N.A.; Ramasamy, A.; Marsadek, M.; Faisal, M.; Hannan, M.A. Review on scheduling, clustering, and forecasting strategies for controlling electric vehicle charging: Challenges and recommendations. *IEEE Access* **2019**, *7*, 128353–128371. [CrossRef]
35. Li, Z.; Ma, T. Peer-to-peer electricity trading in grid-connected residential communities with household distributed photovoltaic. *Appl. Energy* **2020**, *278*, 115670. [CrossRef]
36. Robledo, C.B.; Oldenbroek, V.; Abbruzzese, F.; van Wijk, A.J.M. Integrating a hydrogen fuel cell electric vehicle with vehicle-to-grid technology, photovoltaic power and a residential building. *Appl. Energy* **2018**, *215*, 615–629. [CrossRef]
37. Zahedi, R.; Ghodusinejad, M.-H.; Aslani, A. Modelling community-scale renewable energy and electric vehicle management for cold-climate regions using machine learning. *Energy Strategy Rev.* **2022**, *43*, 100930. [CrossRef]
38. Falces, A.; Capellan-Villacian, C.; Mendoza-Villena, M.; Zorzano-Santamaria, P.J.; Lara-Santillan, P.M.; Garcia-Garrido, E.; Fernandez-Jimenez, L.A.; Zorzano-Alba, E. Short-term net load forecast in distribution networks with PV penetration behind the meter. In *Energy Report, Proceedings of the 2022 3rd International Conference on Power, Energy and Electrical Engineering (PEEE 2022), Barcelona, Spain, 18–20 November 2022*; Elsevier: Amsterdam, The Netherlands, 2023; Volume 9, pp. 115–122. [CrossRef]
39. Tharumaraja, S.; Liyanage, M.P.-P.; Wijethuunge, A.; Ekanayake, J.; Rupasinghe, A. Very Short-Term Surplus Energy Forecasting for Peer-to-Peer Energy Trading in Microgrids. In Proceedings of the IEEE 2025 5th International Conference on Advanced Research in Computing (ICARC), Belihuloya, Sri Lanka, 19–20 February 2025. [CrossRef]
40. Dais, P.G.S.; Brito, T.; Silva, W.R.; Pereira, A.I.; Lopes, L.C.G.; dos Santos, M.F.; Costa, P.; Lima, J. Development of surplus power generation forecast for use by residential loads. In Proceedings of the IEEE 2023 3rd International Conference on Electrical, Computer, Communications and Mechatronics Engineering (ICECCME), Tenerife, Spain, 19–21 July 2023. [CrossRef]
41. Eze, F.; Lee, W.-J.; An, Y.-S.; Joo, H.; Lee, K.-H.; Ogola, J.; Mwabora, J. Development and simulated evaluation of inter-seasonal power-to-heat and power-to-cool with underground thermal storage for self-consumption of surplus solar energy in buildings. *Energy Convers. Manag.* **2024**, *320*, 119013. [CrossRef]
42. Liao, W.; Kim, C.; Xiao, Y.; Kim, H.; Hong, T.; Yin, S.; Heo, Y. Quantifying photovoltaic surplus at an urban scale: A case study in Seoul. *Energy Build.* **2023**, *298*, 113523. [CrossRef]
43. Bhatti, S.; Williams, A. Estimation of surplus energy in off-grid solar home systems. *Renew. Energy Environ. Sustain.* **2021**, *6*, 25. [CrossRef]
44. Zhou, H.; Zheng, P.; Dong, J.; Liu, J.; Nakanishi, Y. Interpretable feature selection and deep learning for short-term probabilistic PV power forecasting in buildings using local monitoring data. *Appl. Energy* **2024**, *376*, 124271. [CrossRef]
45. Li, Y.; Tong, Z.; Tong, S.; Westerdahl, D. A data-driven interval forecasting model for building energy prediction using attention-based LSTM and fuzzy information granulation. *Sustain. Cities Soc.* **2022**, *76*, 103481. [CrossRef]
46. Kutty, N.; Barakat, D.; Khoukhi, M. A French residential retrofit toward achieving net-zero energy target in a mediterranean climate. *Buildings* **2023**, *13*, 833. [CrossRef]
47. EPISCOPE EU. Residential Building Typology. 2013. Available online: https://episcope.eu/building-typology/country/fr/ (accessed on 7 May 2025).
48. DesignBuilder. DesignBuilder Software Ltd. 2025. Available online: https://designbuilder.co.uk/simulation (accessed on 10 March 2025).
49. Aruta, G.; Ascione, F.; Bianco, N.; Mauro, G.M. Sustainability and energy communities: Assessing the potential of building energy retrofit and renewables to lead the local energy transition. *Energy* **2023**, *282*, 128377. [CrossRef]
50. Foda, E.; El-Hamalawi, A.; Le Dreau, J. Computational analysis of energy and cost efficient retrofitting measures for the French house. *Build. Environ.* **2020**, *175*, 106792. [CrossRef]
51. García, A.O. Modeling Solar Thermal Systems with DesignBuilder-EnergyPlus. 2016. Universidad Rovira i Virgili. Available online: https://web.cut.ac.cy/wp-content/uploads/sites/13/2016/04/SolarThermalSystems-DesignBuilder_2016-03-31.pdf (accessed on 10 March 2025).
52. Shahriar, K.; Ali, M.H.; Mahmud, M.-K.; Hossain, M.R. Optimization of combined electricity generation and cooling load reduction by incorporating roof top photovoltaic module: An approach to energy consumption reduction in a hospital building. *Energy Convers. Manag. X* **2025**, *26*, 100948. [CrossRef]
53. Salazar, C.; Banerjee, A.G. A distance correlation-based approach to characterize the effectiveness of recurrent neural networks from time series forecasting. *Neurocomputing* **2025**, *629*, 129641. [CrossRef]
54. Lara-Benitez, P.; Carranza-Garcia, M.; Riquelme, J.C. An experiment review on deep learning architectures for time series forecasting. *Int. J. Neural Syst.* **2021**, *31*, 2130001. [CrossRef] [PubMed]
55. Han, J.; Zeng, P. Residual BiLSTM based hybrid model for short-term load forecasting in buildings. *J. Build. Eng.* **2025**, *66*, 111593. [CrossRef]
56. Aseeri, A.O. Effective RNN-based forecasting methodology design for improving short-term power load forecasts: Application to large-scale power grid time series. *J. Comput. Sci.* **2023**, *68*, 101984. [CrossRef]

57. Bhoj, N.; Bhadoria, R.S. Time-series based prediction for energy consumption of smart home data using hybrid convolution-recurrent neural network. *Telemat. Inform.* **2022**, *75*, 101907. [CrossRef]
58. Jiang, B.; Gong, H.; Qin, H.; Zhu, M. Attention-LSTM architecture combined with Bayesian hyperparameter optimization for indoor temperature prediction. *Build. Environ.* **2022**, *224*, 109536. [CrossRef]
59. Wang, Z.; Hong, T.; Piette, M.A. Building thermal load prediction through shallow machine learning and deep learning. *Appl. Energy* **2020**, *263*, 114683. [CrossRef]
60. Yu, H.; Zhong, F.; Du, Y.; Xie, X.; Wang, Y.; Zhang, X.; Huang, S. Short-term cooling and heating loads forecasting of building district energy system based on data-driven models. *Energy Build.* **2023**, *298*, 113513. [CrossRef]
61. Santos, M.L.; García, S.D.; García-Santiago, X.; Ogando-Martínez, A.; Camarero, F.E.; Gil, G.B.; Ortega, P.C. Deep learning and transfer techniques applied to short-term load forecasting of data-poor buildings in local energy communities. *Energy Build.* **2023**, *292*, 113164. [CrossRef]
62. Maltais, L.-G.; Gosselin, L. Forecasting of short-term lighting and plug load electricity consumption in single residential units: Development and assessment of data-driven models for different horizons. *Appl. Energy* **2022**, *307*, 118229. [CrossRef]
63. Nazififard, M.; Zeynali, S. Analysis of Photovoltaic Panel Integration for Achieving Net-Zero Energy in French Residential Retrofits in a Mediterranean Climate. *E3S Web Conf.* **2024**, *545*, 02006. [CrossRef]
64. Kim, D.; Seomun, G.; Lee, Y.; Cho, H.; Chin, K.; Kim, M.-H. Forecasting building energy and onsite power generation for residential buildings using long and short-term memory method with transfer learning. *Appl. Energy* **2024**, *368*, 123500. [CrossRef]
65. Montavon, G.; Samek, W.; Muller, K.-R. Methods for interpreting and understanding deep neural networks. *Digit. Signal Process.* **2018**, *73*, 1–15. [CrossRef]
66. Hu, Y.; Cheng, X.; Wang, S.; Chen, J.; Zhao, T.; Dai, E. Time series forecasting for urban building energy consumption based on graph convolutional network. *Appl. Energy* **2022**, *307*, 118231. [CrossRef]
67. Goodfellow, I.; Bengio, Y.; Courville, A. *Deep Learning*, 1st ed.; MIT Press: Cambridge, MA, USA, 2016. Available online: https://scholar.google.com/citations?view_op=view_citation&hl=en&user=iYN86KEAAAAJ&citation_for_view=iYN86KEAAAAJ:ZeXyd9-uunAC (accessed on 1 June 2025).
68. Wang, Z.; Wang, Y.; Srinivasan, R.S. A novel ensemble learning approach to support building energy use prediction. *Energy Build.* **2018**, *159*, 109–122. [CrossRef]

Disclaimer/Publisher's Note: The statements, opinions and data contained in all publications are solely those of the individual author(s) and contributor(s) and not of MDPI and/or the editor(s). MDPI and/or the editor(s) disclaim responsibility for any injury to people or property resulting from any ideas, methods, instructions or products referred to in the content.